Pulsar Double-lensing Event Sheds Light on the Origin of Extreme Scattering Events

Hengrui Zhu

an Honors Thesis presented to the Oberlin College
Department of Physics and Astronomy

Advisors: Professors Rob Owen and Dan Stinebring

March 31, 2021

Contents

This work is dedicated to the memory of my mother, Caifeng Liu.

Acknowledgments

First and foremost I am extremely grateful to my supervisors, Prof. Dan Stinebring, Prof. Rob Owen, and Prof. Chris Marx, for their sincerest advice and long-lasting support. Dan has been an invaluable mentor to me since my freshman year at Oberlin; his constant support and guidance have been crucial not only to my research achievements but also my personal well-being. Through the funding from NANOGrav, Dan has supported me to travel the world and interact with many established scientists in the astrophysics community. Rob has been equally influential to me. With a chalk and a blackboard, he brought me to the enchanting world of theoretical physics. I have inherited much of his research attitude, which has helped me to overcome countless challenges. Chris has also been an inspiring mentor. He taught me the strength and beauty of studying physics with rigorous mathematics, which I will embrace for the rest of my career. To them I am forever in debt.

I also want to send my deepest gratitude to Prof. Ue-Li Pen and Prof. Marten van Kerkwijk (Professors at Canadian Institute for Theoretical Astrophysics, University of Toronto), whose mentorship is crucial to the completion of the thesis. Ue-Li's theory and insight have guided me throughout this project. And Marten's elegant simulation works have granted me an opportunity to understand the underlying physics fundamentally. I also want to thank Daniel Baker, who co-developed the theta-theta techniques and guided me hand-by-hand for the implementation. Thanks are also due to my advisors/collaborators: Prof. Barney Rickett, Prof. Timothy Dolch, Dr. James Mckee, Dr. Pei Wang, Dr. Dongzi Li, and Dr. Rik van Lieshout.

Abstract

Extreme scattering events — propagation-produced variations in quasar flux density — have been a puzzle since their discovery in 1987. In brief, models for them require over-pressure in the interstellar gas that should cause them to dissipate in about a year. Pulsar observations, particularly scintillation observations, have long held the promise of elucidating the physical characteristics of the lenses underlying this phenomenon. In this work, we present direct observational evidence for an isolated and anisotropic lens with a width of 1 mas and an upper bound in electron density of 300 cm^{-3}. The required electron density further reduces if the lens is inclined along the line of sight. The lens deflected the radio emission of a pulsar B0834+06 by 80 mas at 318MHz, which inevitably causes an extreme scattering event at 2.7 GHz if the lens moves across the foreground of a quasar.

Chapter 1

Introduction

1.1 Thesis Motivation

The interstellar medium (ISM) plays a significant role in galactic evolution. Despite recent efforts, some aspects of the interstellar medium are still poorly understood. In particular, the ISM structure responsible for observed Extreme Scattering Events (ESE) of quasars remains a mystery (Fiedler et al., 1987). Quasars are extremely bright active galactic nuclei, where gas is accreting to a super massive black hole. ESEs are significant fluctuations of the observed flux in quasars due to a foreground plasma lens in the ISM for a time-span varying from weeks to months (more details in Section 1.3). However, the required free electron density for such a plasma lens needed to explain the observed flux curve seems to imply a high pressure within the lens if we assume the lens to be isotropic. In this work, from analysis of a pulsar double lensing event, we present evidence for an isolated anisotropic plasma lens in the interstellar medium capable of producing an ESE. This is the first such unambiguous detection of an ESE using the powerful tool of scintillation arc analysis.

1.2 Interstellar Medium

The ISM is the matter that exist between stars within a galaxy. ISM is composed of gas in various forms. The ISM in our galaxy contains mostly hydrogen, followed by helium as well as small amounts of carbon, oxygen, and nitrogen. The ISM is crucial in galactic evolution as it fills the gap between the stellar scale and the galactic scale. In particular, stars form in the region of a galaxy with dense ISM, and the gaseous content in the medium determines the star forming rate as well as the lifespan of the galaxy.

We are most interested in the ionized gas, or plasma, in the ISM, as free electrons are the main contributors to a variety of phenomenon that can be probed through radio astronomy. Plasma can be characterized by the plasma frequency $\omega_p = \sqrt{n_e e^2/\epsilon_0 m_e}$, where n_e, e, and m_e are the electron volume density, charge of an

electron, and mass of an electron. The plasma frequency corresponds to the oscillation frequency of electrons subject to a restoring force inside an electrically neutral plasma. The index of refraction of a plasma can be written in terms of the plasma frequency, $n = \sqrt{1 - \omega_p^2/\omega^2} \approx 1 - wp^2/(2w^2)$, as ω, the angular frequency of the electromagnetic wave, is much larger than the plasma frequency. Notice that the index of refraction for plasma is less than 1. This indicates that plasma lenses are divergent. See, e.g. Pen & Levin (2014); Clegg et al. (1998).

1.3 Extreme Scattering Events

Extreme scattering events were first discovered 30 years ago through a daily flux monitoring program of quasars (Fiedler et al., 1987). The ESE manifests as a change in the observed flux of a quasar, usually a dipping, for a period of several weeks to months. It is now widely agreed that ESEs cannot be explained by intrinsic variations of the source. Instead, refraction effects from a dense structure in the ISM with a length scale of a few astronomical units[1] can explain both the observed flux curve as well as duration of such events (Clegg et al., 1998), where the refraction is caused by free electrons in the ISM.

One difficulty remains: the required electron density, $n_e \approx 10^3$ cm^{-3}, and temperature, $T \approx 10^4$K, for such a lens implies a pressure of $P = NkT/V \approx 10^{-10}$Pa, which exceeds the pressure in the diffusive ISM by a factor of 10^3 (Walker & Wardle, 1998; Goldreich & Sridhar, 2006). Such a high pressure indicates that the proposed plasma lens would evaporate on the time scale of a year. This is known as the over-pressure problem.

Several theoretical models have been proposed to address this problem: Romani (1988) argue that the proposed lenses may only exist in regions with high pressure in the ISM — specifically, old supernova shocks; Walker & Wardle (1998) propose that the lenses could be the ionized skin of cold, self-gravitating cloud of gas, where the self-gravitation balances the required pressure; last but not least, Pen & King (2012) propose highly inclined current sheets, likely caused by magnetic reconnection, where the projected electron density is dramatically increased when we view the sheet edge-on.

Attempts have been made to directly image these lenses through VLBI[2] observations of quasar ESEs (Fey et al., 1996; Pushkarev et al., 2013). However, due to the finite angular size of quasars, ~ 10 milliarcseconds (mas) at 2 GHz, the structure of the ISM lens remains unresolved. The same structure is thought to be responsible for multiple imaging of pulsars (Cordes & Wolszczan, 1986; Rickett et al., 1997), where, due to the point source nature of pulsars, the lens can potentially be resolved.

[1] An astronomical unit (AU) is the mean Earth-Sun distance.

[2] VLBI, or Very Long Baseline Interferometry, is a technique to conduct simultaneous observation a source with several telescopes. The recorded baseband data, or the time samples of the complex electric field, from different telescopes are then cross correlated before forming the spectra. We refer the reader to Condon & Ransom (2016) a basic theory of VLBI.

1.4 Pulsars and Pulsar Scintillation

Neutron stars are stellar remnants of massive stars (with 10–25 solar mass) formed in supernova explosions. With a mass of two times that of our sun packed in a diameter of 15 km, they are the densest known stellar object in the universe (Heger et al., 2003). Pulsars are rapidly spinning and highly magnetized neutron stars that radiate, primarily in the radio portion of the electromagnetic spectrum. Their radiation beams sweep across the sky much like a lighthouse: if their beams sweep past the Earth every rotation, we then detect periodic pulses with a radio telescope (Lorimer & Kramer, 2005).

Because of their extremely compact angular size ($\sim 10^{-16}$ radians), pulsars scintillate at radio frequency due to the inhomogeneity of the interstellar medium (ISM), just like stars scintillate due to turbulence in the atmosphere(Rickett, 1990; Cordes et al., 2006). Pulsar scintillation has been used to study the interstellar medium (ISM) since the 1970s (Lee, 1976; Rickett, 1977). Due to their incredibly small angular sizes, pulsars can resolve structures in the ISM at the scale of the solar system (Hill et al., 2005; Simard & Pen, 2018; Brisken et al., 2010). To explain the observed scintillation effects, some models proposed a volume-filling turbulent medium (Rickett, 1990). However, the subsequent discovery of scintillation arc (Stinebring et al., 2001) provided evidence for discrete scattering region along the line of sight that can be well-modeled by a thin screen (see section 2.2 for details).

A schematic for thin screen scattering of a pulsar is given in Figure 1.1. The inhomogeneity of the free electron density inside the screen yields a distortion in the wavefronts of the pulsar radiation. This distortion of the wavefronts then induces spatial intensity modulations far enough from the screen. The resulting intensity modulation, known as the diffraction pattern, is projected onto a plane at the Earth perpendicular to the line of sight (LOS). As the system moves, the diffraction pattern sweeps past Earth with a velocity determined by relative transverse motions of the pulsar, screen material, and Earth (Cordes & Rickett, 1998). Hence, if a radio telescope points towards that pulsar, it will record changes in the pulsar's flux as a function of time and frequency, known as a dynamic spectrum. The rest of thesis will focus on detailed analysis of such dynamic spectra.

1.5 Coming Attractions

The organization of this thesis is as follows. In Chapter 2, I discuss the observables and lay out the theory for pulsar scintillation and scintillation arcs. In Chapter 3, I introduce novel analysis techniques for the study of scintillation arcs. In Chapter 4, I present the observation and analysis for the pulsar B0834+06 double lensing event. I present an overview of my results in Chapter 5 with a discussion of future work.

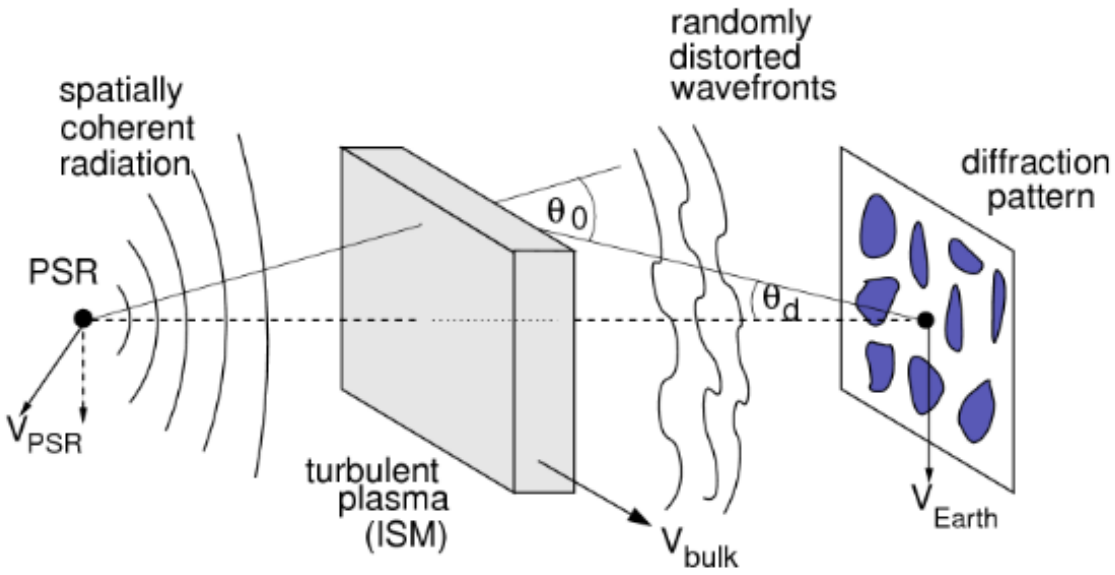

Figure 1.1: A schematic of pulsar scintillation (Lorimer & Kramer, 2012).

Chapter 2

Observables and Interpretations of Pulsar Scintillation

2.1 Dynamic Spectrum

In this thesis we mainly study strong scattering scenarios, where the pulsar is scattered into several images. In this regime, the full wave optics picture, which requires the complicated Kirchhoff diffraction integral, can be reduced to ray optics. (Walker et al., 2004). Furthermore, we assume the pulsar is scattered by a single screen unless noted otherwise.

In this section we provide a heuristic derivation of the dynamic spectrum when a finite number of rays are interfering with one another. As defined in section 1.4, the dynamic spectrum is the flux of a pulsar as a function of frequency and time. Recall that the variation in the observed pulsar flux is caused by the motion of the diffraction pattern with respect to Earth. In the ray optics limit, the diffraction pattern becomes the interference of a finite number of rays. For example, if there are only two scattered images of the pulsar visible on the sky, the diffraction pattern will simply reduce to that of double slit interference. For double slit interference, in the far-field limit, the spatial wavelength of modulation at a distance $d_{\rm screen}$ is given by:

$$\boldsymbol{\Lambda} \equiv \frac{d_{\rm screen}\lambda}{d}\hat{\boldsymbol{d}}\,, \tag{2.1}$$

where d is the spatial separation between the slits, and $\hat{\boldsymbol{d}}$ is a unit vector indicating the direction of separation. In our case, $d_{\rm screen}$ is the distance between the ISM screen and Earth (see Figure 2.1), typically on a length scale of 100 parsec (or roughly 2×10^5 AU, the average distance between Earth and the Sun), whereas d, the spatial distance between two scattered images, is roughly 10 AU. Hence, we may apply the small angle approximation and further write:

$$\boldsymbol{\Lambda} = \frac{d_{\rm screen}\lambda}{d}\hat{\boldsymbol{d}} = \frac{\lambda}{\Delta\theta}\hat{\boldsymbol{d}}\,, \tag{2.2}$$

where $\Delta\theta$ is the observed angular separation between the two images.

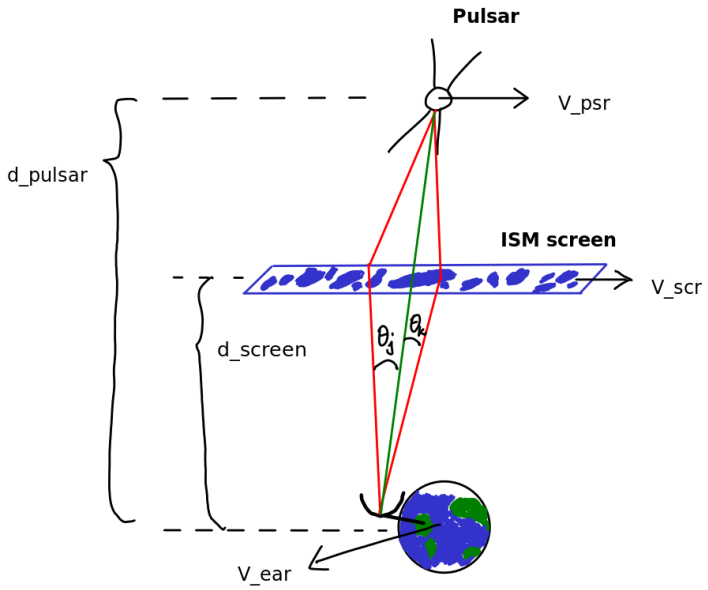

Figure 2.1: A schematic for thin screen scattering. The green ray represents the line-of-sight image of the pulsar, and the two red rays represent two scattered images of the pulsar.

In short, the interference between every pair of the images contributes a sinusoidal component to the diffraction pattern with a certain spatial wavelength. Then, as the system moves, a spatial sinusoidal variation in the intensity translates to a temporal sinusoid in a dynamic spectrum. The temporal frequency of this sinusoidal variation can be characterized by the following:

$$f_{\rm t} = \frac{\mathbf{V}_{\rm eff}}{|\mathbf{\Lambda}|} \cdot \hat{\mathbf{\Lambda}} = \frac{\mathbf{V}_{\rm eff} \cdot (\boldsymbol{\theta}_{\mathbf{k}} - \boldsymbol{\theta}_{\mathbf{j}})}{\lambda} \ , \tag{2.3}$$

where $\boldsymbol{\theta}_k$ and $\boldsymbol{\theta}_{\boldsymbol{j}}$ are the angular positions of the two images; λ is the observing wavelength, and $\mathbf{V}_{\rm eff}$ is the effective velocity of the diffraction pattern with respect to Earth, see e.g. Stinebring et al. (2001); Simard & Pen (2018). The effective velocity can then be written as:

$$\mathbf{V}_{\rm eff} = \mathbf{V}_{\rm psr} \frac{1-s}{s} - \frac{\mathbf{V}_{\rm scr}}{s} + \mathbf{V}_{\rm Earth} \ , \tag{2.4}$$

where $\mathbf{V}_{\rm psr}$, $\mathbf{V}_{\rm scr}$, and $\mathbf{V}_{\rm Earth}$ are respectively the pulsar velocity, screen velocity, and Earth velocity. s is the fractional screen distance defined by

$$s = 1 - \frac{d_{\rm screen}}{d_{\rm psr}} \ , \tag{2.5}$$

where $d_{\rm screen}$ and $d_{\rm psr}$ are the distance to the ISM screen and pulsar from Earth. A schematic demonstrating these quantities is given in Figure 2.1.

It is then logical to ask how such a diffraction pattern changes with frequency. It can be shown that the intensity of the interference between a pair of images also varies sinusoidally as a function of frequency, with

period:

$$f_\nu = \frac{D_{\rm eff}(\theta_j^2 - \theta_k^2)}{2c} \ , \tag{2.6}$$

$$\text{with } D_{\rm eff} = d_{\rm psr}\frac{1-s}{s} \ , \tag{2.7}$$

and c the speed of light (Stinebring et al., 2001). Therefore, each pair of scattered images creates a 2-d sinusoid in the dynamic spectrum.

Some important physical interpretations can more readily be extracted from f_t and f_ν if we take $\theta_k = 0$, i.e., one of the images is the line-of-sight image. Specifically, f_t then represents the relative Doppler frequency between the scattered image θ_j and the line-of-sight image, and f_ν becomes the relative geometric delay of θ_j with respect to the line-of-sight image.

$$f_{Dj} = f_{\rm t}(\theta_k = 0) = -\frac{\mathbf{V}_{\rm eff}\cdot\boldsymbol{\theta}_{\mathbf{j}}}{\lambda} \ , \tag{2.8}$$

$$\text{and} \quad \tau_j = f_\nu(\theta_k = 0) = \frac{D_{\rm eff}\theta_j^2}{2c} \ . \tag{2.9}$$

We show a simulation of the dynamic spectrum in Figure 2.2. When there are two images (a scattered image and the line-of-sight image), the dynamic spectrum is a 2D sinusoid. As the number of images N increases, the dynamic spectrum appears to be more stochastic, as the number of sinusoidal components increases as N factorial (Figure 2.3), and the phase of the sinusoids are, in general, uncorrelated. An observed dynamic spectrum is given in Figure 2.4 for comparison.

2.2 Secondary Spectrum and Scintillation Arcs

The secondary spectrum is defined as the square modulus of the 2D Fourier transform of the dynamic spectrum. The axes are then given by the conjugate variables of time and frequency, namely relative delay and Doppler frequency as defined in Eqn 2.6 and 2.3. The interference between a pair of images, which is a 2D sinusoidal function in the dynamic spectrum, is represented by two delta functions in the secondary spectrum, symmetric about the origin. Note that the secondary spectrum is symmetric as the dynamic spectrum is entirely real.

A model of scintillation arcs has been developed in (Stinebring et al., 2001; Cordes et al., 2006; Walker et al., 2004), which we summarize here. In a single screen geometry, the relative delay (conjugate variable of frequency) between each image and the line of sight image is proportional to square of their angular separation when viewed by the observer, whereas the relative Doppler shift (conjugate variable of time) between the images is proportional to the angular separation. Hence, the thin screen geometry results in a parabolic arc in the secondary spectrum, which we refer to as the scintillation arc. The scintillation arc is given by Eqn 2.6 and 2.3, which we repeat here:

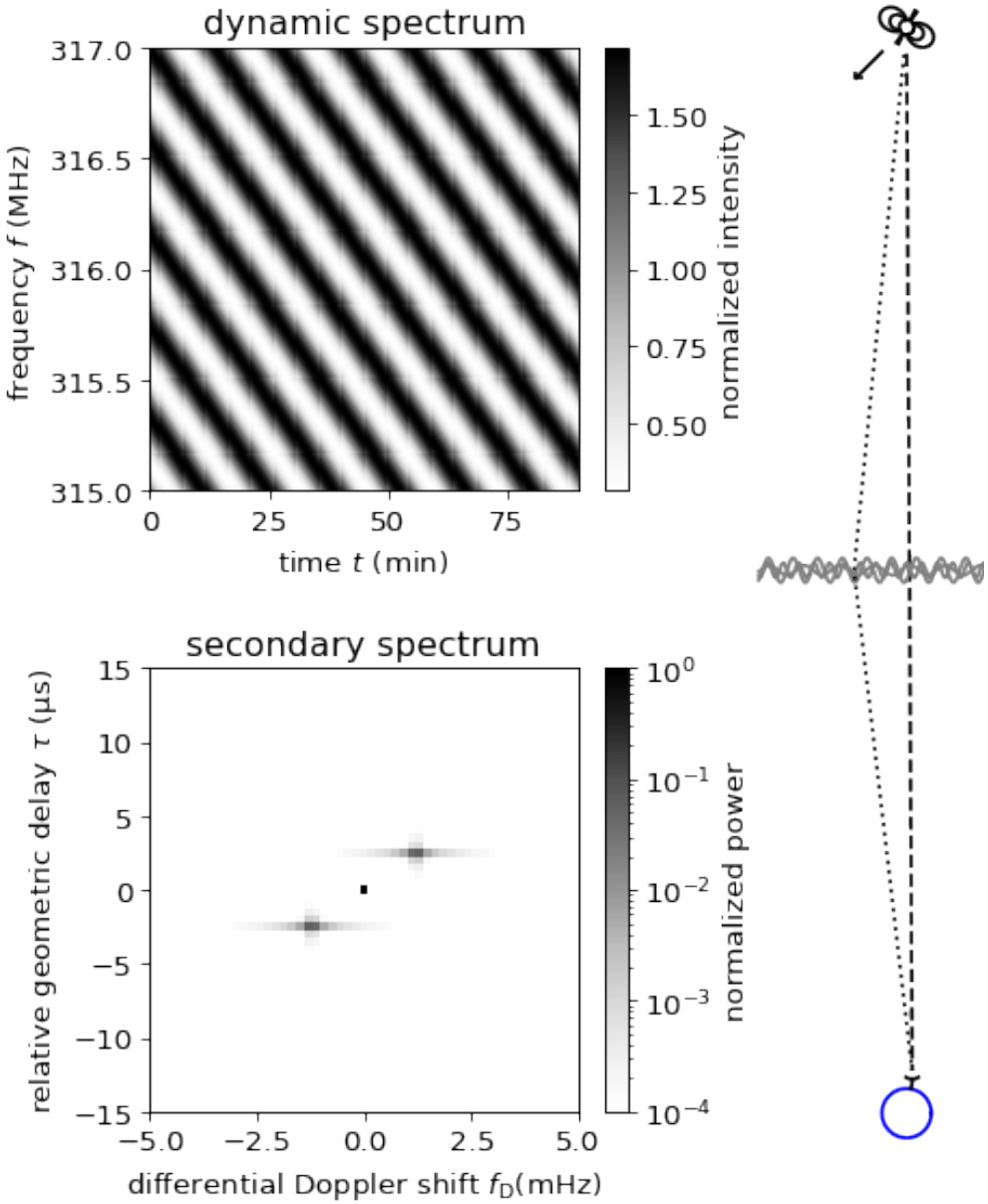

Figure 2.2: Simulation of two scattered images. The top left panel shows the dynamic spectrum, in which the intensity is a 2D sinusoid. Simulation credit: Dr. Marten van Kerkwijk and Dr. Rik van Lieshout at CITA.

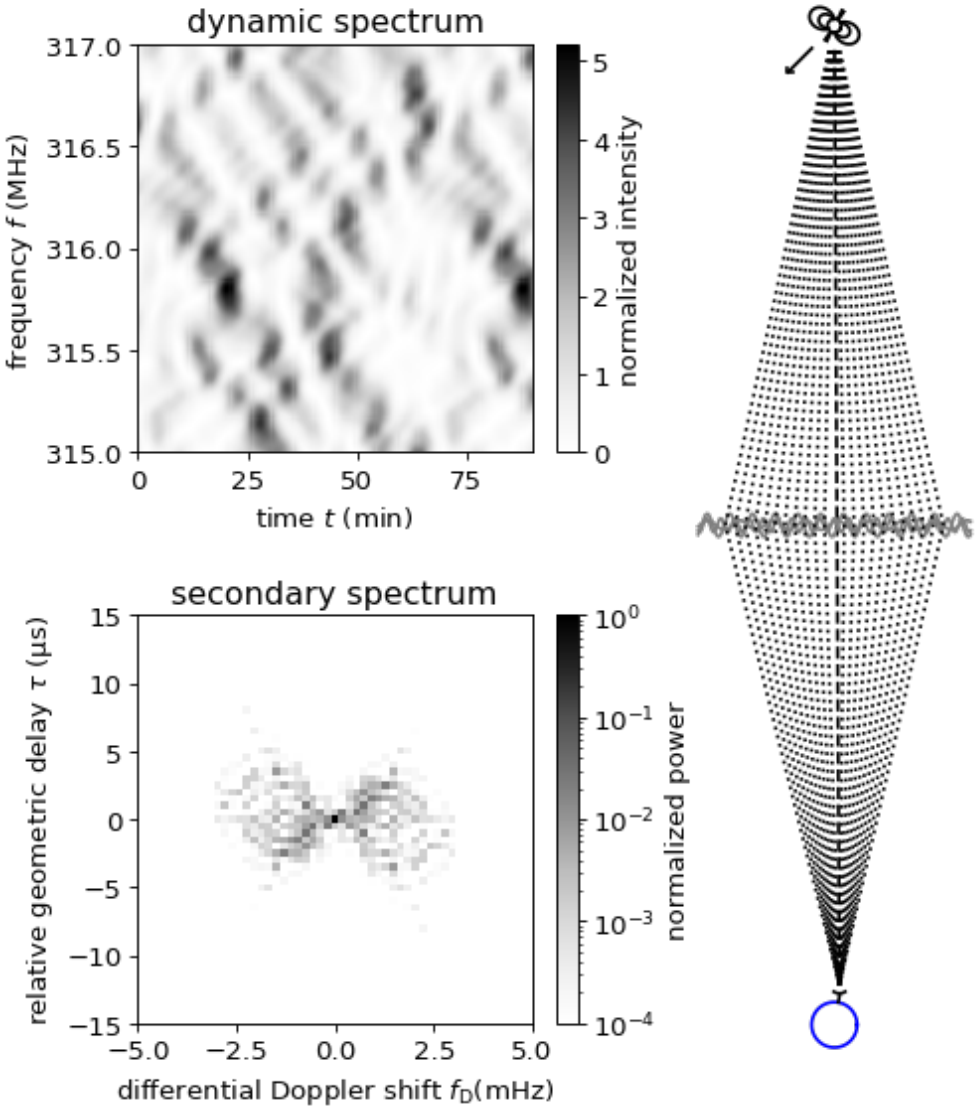

Figure 2.3: Simulation of many scattered images. The dynamic spectrum appears to be stochastic. Simulation credit: Dr. Marten van Kerkwijk and Dr. Rik van Lieshout at CITA.

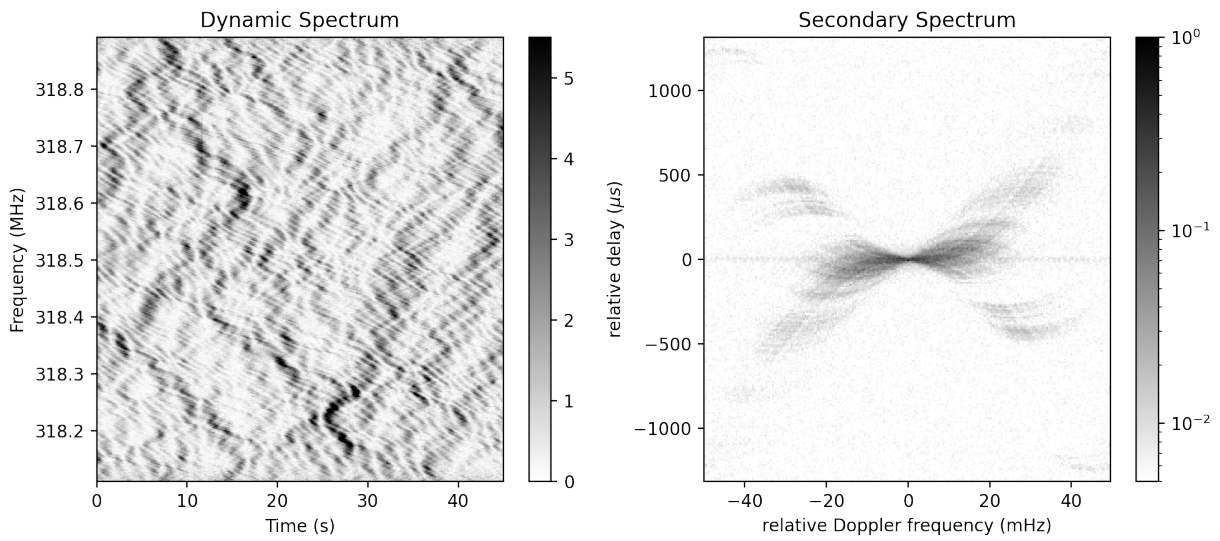

Figure 2.4: Dynamic and secondary spectrum of B0834+06 on MJD 53665. Observation by Dr. Dan Stinebring at Arecibo Observatory.

$$\tau = f_\nu = \frac{D_{\text{eff}}}{2c}(\boldsymbol{\theta}_j^2 - \boldsymbol{\theta}_k^2) \ , \tag{2.10}$$

$$f_D = f_t = \frac{1}{\lambda}(\boldsymbol{\theta}_k - \boldsymbol{\theta}_j) \cdot \mathbf{V}_{\text{eff}} \ . \tag{2.11}$$

Much observational evidence points towards highly anisotropic scattering, i.e. the scattered images lie along a straight line, see e.g. (Pen & Levin, 2014; Brisken et al., 2010; Rickett et al., 2021). While the astrophysical mechanism for producing such highly anisotropic scattering is still unknown, an a simple, illustrative model was proposed in Pen & Levin (2014). They pointed out that refraction from a corrugated sheet of plasma at a grazing angle is analogous to the reflection of the sun on the ocean near sunset. In the absence of waves, exactly one image forms with the angle of incidence equal to the angle of reflection; in the presence of waves, a linear groups of images form on the wave crests (Figure 2.5). Similarly, refraction by a corrugated sheet also leads to anisotropic images (Figure 2.6).

Assuming that the scattering is highly anisotropic, and that the angle between the resulting linear image and the effective velocity is α, it is clear from equation (2.10) and (2.11) that the curvature of the scintillation arc is then given by

$$\eta = \frac{D_{\text{eff}}\lambda^2}{2cV_\alpha^2} \ , \text{ where} \tag{2.12}$$

$$V_\alpha = |\mathbf{V}_{\text{eff}}| \cos\alpha \ . \tag{2.13}$$

A simulation of the secondary spectrum for a single pair of scattered images is shown in 2.2: when there are only two images (a scattered image and the line-of-sight image), the secondary spectrum is zero except

Figure 2.5: Reflection of the sun at sunset forms a linear image. Photo credit: Michiko Kumai, Digital Camera Magazine

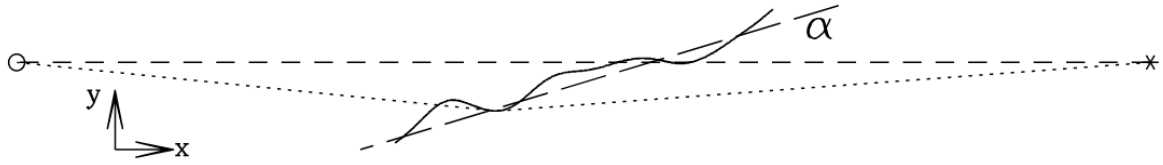

Figure 2.6: Lensing geometry from a corrugated sheet (adapted from Pen & Levin (2014)). The earth is at the left, the pulsar at the right. A section of the corrugated scattering sheet is plotted in the middle as the solid curve. The dashed line shows the unperturbed light path. The dotted line shows the path of an image produced by a fold singularity of the projected sheet, analogous to a reflected image produced on a wave in Figure 2.5.

for two points symmetric about the origin corresponding to the periodicity to the 2D sinusoid in the time domain (dynamic spectrum). As the number of images increases, we observe that the secondary spectrum becomes much denser (Figure 2.3), yet its power still concentrates along a parabola. An observed secondary spectrum of pulsar B0834+06 is given in Figure 2.4 for comparison.

2.3 The origin of inverted arclets

Note that in both simulation and real data (Figure 2.3 and 2.4), the power in the secondary spectrum does not lie only on a parabola; instead, there is a myriad of inverted parabolas with their apex lying on a forward parabolic arc. These inverted parabolas are known as inverted arclets. They are formed by one scattered image interfering with all the rest of the images (Walker & Stinebring, 2005). Fixing θ_j, we may then rewrite equations 2.11 and 2.10 as:

$$\tau(\boldsymbol{\theta}_k) = \tau_j - \frac{D_{\text{eff}}}{2c}(\boldsymbol{\theta}_k^2) \ , \tag{2.14}$$

$$f_D(\boldsymbol{\theta}_k) = f_{Dj} + \frac{1}{\lambda s}\boldsymbol{\theta}_k \cdot \mathbf{V}_{\text{eff}} \ \ , \tag{2.15}$$

where τ_j and f_{Dj} are defined as the relative delay and relative Doppler frequency of $\boldsymbol{\theta}_j$ with respect to the line-of-sight image in Eqn 2.9 and 2.8.

Note that if the the scattering is linear, meaning $\boldsymbol{\theta}_k$ is constrained to move along a straight line, hence treated as a one-dimensional numerical parameter, we may view the two equations above as x and y components of a curve parametrized by θ_k in the secondary spectrum. It can then be further simplified:

$$\tau - \tau_j = -\eta(f_D - f_{Dj})^2 \ . \tag{2.16}$$

This curve is exactly an inverted arclet, i.e. a parabola with curvature $-\eta$ and its apex on (f_{Dj}, τ_j), where η is the curvature of the main scintillation arc as defined in 2.12. This arclet is hence a result of the image $\boldsymbol{\theta}_j$ interfering with all other images in highly anisotropic scattering scenarios.

2.4 Temporal Motion of Arclets

A scattered image of the pulsar is physically associated with a plasma lens embedded in the ISM screen (Hill et al., 2005). A plasma lens could arise from an over-dense region in a turbulent medium (Rickett, 1990), a fold on a corrugated sheet (Pen & Levin, 2014), or a photo-ionized surface of cold self-gravitating gas cloud (Walker & Wardle, 1998). Regardless of its origin, such lenses would remain practically stationary with respect to the ISM screen on a time scale of interest to us, $\lessapprox$ 100 days.

Assuming a geometry for a lens (linear, or round pebble), we may predict how the associated scattered image moves with respect to the line-of-sight image as the system moves. (By "the system", we mean the

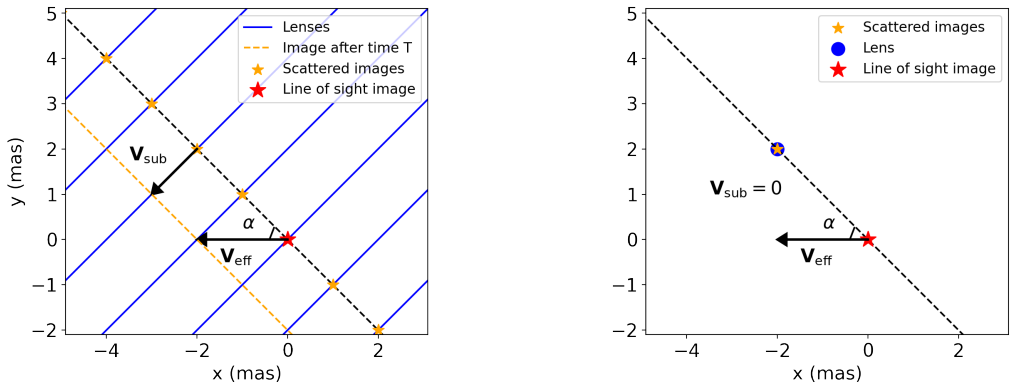

Figure 2.7: Two lens models. Linear lens (Left), round lens (Right)

pulsar - ISM screen - Earth system.) This inferred relative motion then predicts a temporal evolution of some structure in the secondary spectrum. Specifically, the trajectory of the arclet associated with the scattered image in the secondary spectrum can be predicted. In this section, we analyze the predicted arclet's motion in two lensing models, namely a highly anisotropic (linear) lens or a round pebble lens.

2.4.1 Highly anisotropic lens

We refer the readers to Clegg et al. (1998) for the theoretical details of a plasma lens. By highly anisotropic lens, we mean that the gradient of its electron density is much larger in one direction than the direction perpendicular to it. As predicted in Pen & Levin (2014) and Gwinn (2019), these lenses extend linearly in one direction and exist in a large group where all lenses are parallel (see left panel of Figure 2.7). For the discussion below, we treat the lenses to be completely linear so that they can only bend light in the direction perpendicular to their long axis (where it has non-zero gradient in electron density).

In the case where the lenses are linear, the scattered images of the pulsar are also linear and take on a preferred orientation, like viewing the reflection of a light on the rippling surface of a lake at almost grazing angle (Pen & Levin, 2014; Liu et al., 2016). In this scenario, the orientation of the images would be perpendicular to that of the lenses. As the system moves, each scattered image is constrained to move on the lens responsible for it. An illustration is given in Figure 2.7.

If the pulsar's line-of-sight image moves at an apparent velocity $\mathbf{V}_{\rm app}$ with respect to the lens, then the scattered image moves at a speed $\sin(\alpha)|\mathbf{V}_{\rm app}|$ along the lens, where α is the angle between the orientation of the image and $\mathbf{V}_{\rm app}$. Define this velocity associated with the scattered image to be $\mathbf{V}_{\rm sub}$ (see Figure 2.7). Note that the apparent velocity is related to the effective velocity, the velocity of the diffractive pattern with respect to Earth, by the following:

$$\mathbf{V}_{\rm app} = s\mathbf{V}_{\rm eff} = (1-s)\mathbf{V}_{\rm psr} - \mathbf{V}_{\rm scr} + s\mathbf{V}_{\rm Earth} \ , \tag{2.17}$$

where s is the fractional screen distance defined in Eqn 2.5. Let the x-direction be defined by $\mathbf{V}_{\rm app}$; then, the relative angular velocity between the subimage and the line-of-sight image is

$$\dot{\theta}_x = \frac{|(\mathbf{V}_{\rm app} - \mathbf{V}_{\rm sub}) \cdot \hat{x}|}{(1-s)d_{\rm psr}} = \frac{\cos^2(\alpha)|\mathbf{V}_{\rm app}|}{(1-s)d_{\rm psr}} \ , \tag{2.18}$$

On the other hand, θ_x can also be expressed by taking a time derivative in Eqn 2.8:

$$\dot{\theta}_x = \frac{\dot{f}_D \lambda}{|\mathbf{V}_{\rm eff}|} \ . \tag{2.19}$$

Setting the two equations equal, we can get:

$$\begin{aligned} \dot{f}_D &= \frac{s\cos^2(\alpha)|\mathbf{V}_{\rm eff}|^2}{\lambda(1-s)d_{\rm psr}} \\ &= \frac{\lambda}{2c}\frac{1}{\eta} \ , \end{aligned} \tag{2.20}$$

where η is the curvature of the scintillation arc in Eqn 2.12. Recall that f_D is the relative Doppler frequency of a scattered image with respect to the line-of-sight image, hence the x coordinate for the apex of an arclet.

Since we can measure the curvature of the scintillation arc, we can predict the motion of arclets based on the curvature measurement alone under such model. It remains challenging, however, to measure the curvature of the scintillation arc to the desired precision, given all the rich arclet structure in the spectrum (right panel of Figure 2.4). In section 3.1, we discuss a powerful tool which yields precise curvature measurement in the regime of highly anisotropic scattering.

2.4.2 Round pebble lens

In the case where a scattered image arises from a small ($\sim$ 1 AU) round lens fixed in the screen, as predicted in Walker & Wardle (1998), its motion is constrained to that of the screen. Therefore, the apparent velocity of the scattered image $\mathbf{V}'_{\rm sub} = 0$ in the screen's frame. If such an image is separated from the pulsar's line-of-sight image in the y direction, it would always exhibit a finite delay in the secondary spectrum. The minimum geometric delay is determined by the impact parameter α:

$$\tau_{\rm min} = \frac{D_{\rm eff}\theta^2_{\rm min}}{2c} = \frac{D_{\rm eff}\left(\frac{\alpha}{d_{\rm screen}}\right)^2}{2c} = \frac{\alpha^2}{2cs(1-s)d_{\rm psr}} \ . \tag{2.21}$$

Unless the pebble lens lies exactly on the pulsar's trajectory, the corresponding image would travel along a parabola in the secondary spectrum offset from the origin by a finite delay. This contradicts the observed secondary spectra of pulsar B0834+06, which do not contain significant power at non-zero delays along $f_D = 0$. See Figure 2.4 for an example. In comparison, in the linear lens scenario, a scattered image always travels through the line of sight, or the origin in the secondary spectrum, at some time (Figure 2.7).

Chapter 3

Analysis Techniques

3.1 Theta-Theta Mapping

In the case of highly anisotropic scattering, one can estimate the 1-D brightness function through the theta-theta mapping, a nonlinear mapping that allows for a factorization of the secondary spectrum (Baker et al., 2021, submitted; Sprenger et al., 2021; Rickett et al., 2021). The brightness function is the observed brightness of the pulsar as a function of angle on the sky. When using a single antenna, the brightness function is not a direct observable. However, under the assumptions of a thin scattering screen and highly anisotropic images, the observed scintillation pattern in the dynamic spectrum allows for holographic imaging[1]. The result of interstellar holography is the 1-D brightness function of the pulsar.

Theta-theta mapping is a non-linear coordinate transform of the secondary spectrum. The two coordinates in a secondary spectrum are the relative Doppler frequency f_D and geometric delay τ. To more readily extract angular dependence of the pulsar's brightness function, we define the following coordinate mapping from the sky angle θ_+ and θ_- into f_D and τ:

$$f_D(\theta_+, \theta_-) = \frac{V_\alpha}{\lambda}(\theta_+ - \theta_-) \ , \tag{3.1}$$

$$\text{and} \quad \tau(\theta_+, \theta_-) = \frac{D_{\text{eff}}}{2c}(\theta_-^2 - \theta_+^2) \ , \tag{3.2}$$

$$\text{where } V_\alpha = |\mathbf{V}_{\text{eff}}| \cos\alpha \ , \tag{3.3}$$

and α is the angle between the effective velocity and the orientation of the image. To better visualize the mapping, we present the images of straight lines with constant delay and Doppler frequency under the coordinate transformation in Figure 3.1.

[1] Traditionally in holography, we collect the two dimensional diffractive pattern from a coherent and monochromatic light source (laser) to image the aperture; yet in pulsar scintillation, we record a diffractive pattern in one spatial dimension (from the temporal motion in the system) and one frequency dimension. The unscattered pulsar image serves as the coherent reference beam for the observation.

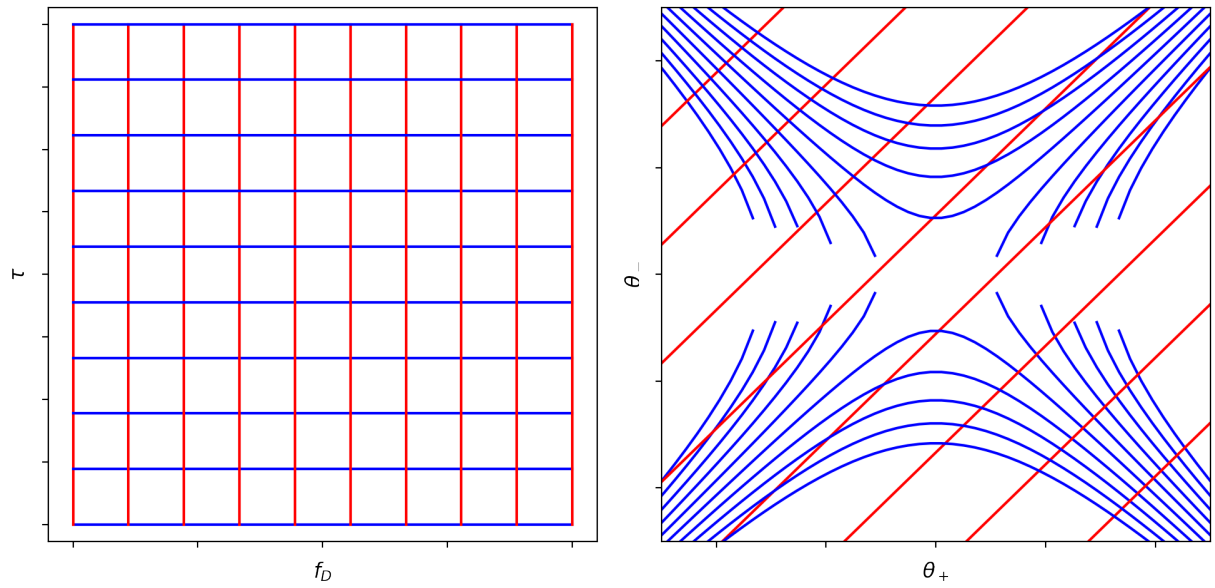

Figure 3.1: Lines with constant delay and Doppler frequency under the theta-theta mapping. We note that constant delays are mapped to hyperbolas, whereas constant Doppler shifts are mapped to straight lines parallel to the diagonal.

We may also write θ_+ and θ_- in terms of f_D and τ:

$$\theta_\pm = -\frac{\lambda}{2V_\alpha}\left(\frac{1}{\eta}\frac{\tau}{f_D} \mp f_D\right) \ . \tag{3.4}$$

Note that the definitions of $\theta_\pm$ are dependent on η the curvature of the scintillation arc. This η-dependence allows us to accurately measure the curvature of the scintillation arc, which we will discuss in detail in section 3.2.

The result of the mapping is referred to as the theta-theta spectrum, $I(\theta_+, \theta_-)$, and is given below, including the determinant of the Jacobian for the transformation $\left|2\sqrt{\eta} f_D\right|$ for flux preservation:

$$I(\theta_+, \theta_-) \equiv S_2(f_D, \tau)\left|2\sqrt{\eta} f_D\right|, \tag{3.5}$$

$$\approx B(\theta_+)B(\theta_-) \ , \tag{3.6}$$

where $S_2(f_D, \tau)$ is the secondary spectrum and $B(\theta)$ is the one-dimensional brightness function. The last step is only valid if the scattering is highly anisotropic. Note that, inherited from the secondary spectrum, $I(\theta_+, \theta_-)$ is ensured to be Hermitian, i.e. $I(\theta_+, \theta_-) = \overline{I(\theta_-, \theta_+)}$. Intuitively, in the regime of 1-D scattering, the theta-theta spectrum encodes the intensity of the interference from all pairs of scattered images, i.e. θ_+ and θ_-.

Under such a mapping, an inverted arclet, formed by one scattered image at θ_j interfering with the rest (Walker et al., 2004; Walker & Stinebring, 2005; Brisken et al., 2010; Simard & Pen, 2018), is mapped to two

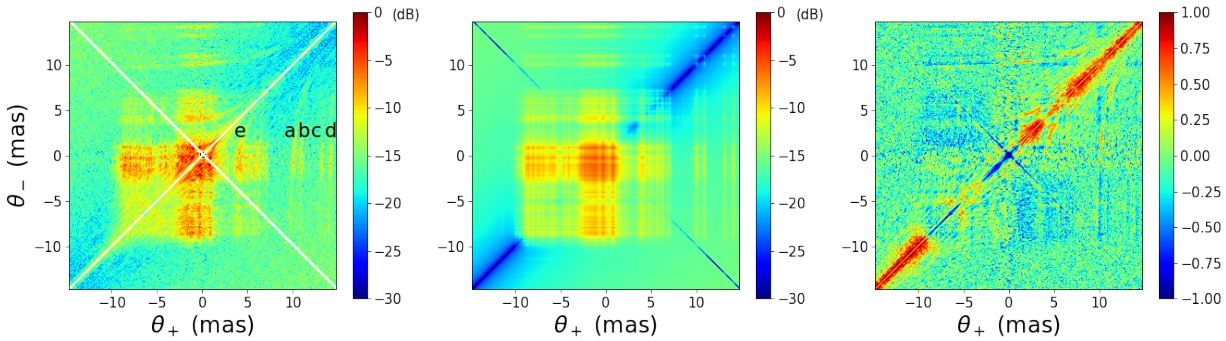

Figure 3.2: θ-θ spectrum of interstellar scintillation at 325 MHz from B0834+06 on MJD 53004. The intensity is displayed on a logarithmic (decibel) scale, and angles are express in milliarcseconds. Left observation; Middle outer product of the 1-D model + mean of noise; Right fractional residual = (observation - model)/max(observation,model).

mutually orthogonal straight lines: $\theta_+ = \theta_j$ and $\theta_- = \theta_j$. This is made clear by the following calculation. The exact equation for an inverted arclet is given in Eqn 2.16. We may then substitute Eqn 3.1 and 3.2 into Eqn 2.16, and get:

$$\frac{D_{\rm eff}}{2c}(\theta_-^2 - \theta_+^2) - \tau_j = -\eta\left[\frac{V_\alpha}{\lambda}(\theta_+ - \theta_-) - f_{Dj}\right]^2 \tag{3.7}$$

$$\frac{D_{\rm eff}}{2c}(\theta_-^2 - \theta_+^2) = -\eta\frac{V_\alpha^2}{\lambda^2}(\theta_+ - \theta_-)^2 + 2\eta f_{Dj}\frac{V_\alpha}{\lambda}(\theta_+ - \theta_-) \tag{3.8}$$

$$\theta_-^2 - \theta_+^2 = -(\theta_+ - \theta_-)^2 + 2\theta_j(\theta_+ - \theta_-) \tag{3.9}$$

$$\theta_-(\theta_- - \theta_j) = \theta_+(\theta_- - \theta_j) \tag{3.10}$$

$$\theta_- = \theta_+ \ , \quad \text{or} \quad \theta_- = \theta_j \ . \tag{3.11}$$

Because the theta-theta spectrum is Hermitian, $\theta_- = \theta_j$ implies $\theta_+ = \theta_j$, with θ_j defined in Eqn 2.8. Note that the entire diagonal line $\theta_- = \theta_+$ is mapped from the origin in the secondary spectrum due to the non-linear mapping. Hence, it does not contain any information.

An example of a theta-theta spectrum of B0834+06 is presented in the left panel of Figure 3.2. It defines $I(\theta_+, \theta_-)$ in a square region bounded by $\pm\theta_{\rm max} = \sqrt{2c\tau_{\rm nyq}/D_{\rm eff}}$, where $\tau_{\rm nyq} = 320\,\mu$s is the Nyquist value in delay.

Considering a square region as in Figure 3.2, we assume that the function I in the square region is a quadratic form in the coordinates $\theta_\pm$. Hence, to recover its principal axes, we can write an eigenvalue problem for the matrix defining that quadratic form. We solve for $B(\theta)$ as its first eigenvector and show the corresponding model, the outer product of $B(\theta)$ with itself, in the middle panel. We justify the above estimation for $B(\theta)$ in subsection 3.1.1. Notice that the noise floor is no longer uniform in the observed

theta-theta spectrum (left panel) because of the extra scaling by the Jacobian through the mapping Eqn 3.5. So, we estimate the noise floor from a region in the secondary spectrum far from any scintillation signature and remove it from the observed spectrum before solving for the eigenvector. The noise floor is then added back into the model. We then compute the residual difference between the observed mapping $I(\theta_+, \theta_-)$ and this model. The right panel shows the residual normalized by the maximum of the data and model at each pixel.

If the scattered image is truly one-dimensional, then Eqn 3.6 implies that the $\theta - \theta$ spectrum becomes the outer product of the brightness function with itself. Such a spectrum has only one eigenvector, namely the brightness function multiplied by a scaling factor. Hence, in the case of linear scattering, this is an exact extraction of the 1-D brightness function from the $\theta - \theta$ spectrum.

3.1.1 Justification for the 1-D brightness estimation as the first eigenvector

The estimation of the 1-D brightness function as the first eigenvector of the theta-theta spectrum is equivalent to a least squares fitting problem directly in the secondary spectrum, first used in Stinebring et al. (2019). The least square fit is formulated as $S_{ij} = B_i B_j + \sigma_{ij}$, where S_{ij} is pixel in the secondary spectrum corresponding to the interference between two scattered images θ_i and θ_j, and B_i, $i = 1, ..., N$ are the N parameters, corresponding to the intensity of θ_i, we are fitting. The squared residual can be written as

$$R \equiv \sum_{i,j} r_{ij}^2 = \sum_{i,j} (S_{ij} - B_i B_j)^2. \tag{3.12}$$

Introducing a constant λ such that

$$B_i = \sqrt{\lambda} v_i \ \forall i,$$

with a normalization constraint on v_i:

$$\sum_{i=1}^{N} v_i^2 = 1 \ .$$

For the residual to be at a minimum yet still satisfying the normalization constraint, we necessarily need

$$\frac{\partial R}{\partial v_k} = 0 \ , \ \forall k \ . \tag{3.13}$$

Hence, following from Eqn 3.12 and 3.13, we obtain a set of equations, :

$$\begin{aligned}
\frac{\partial R}{\partial v_k} &= \sum_{i,j} 2(S_{ij} - \lambda v_i v_j)(-\lambda(\delta_{i,k} v_j + \delta_{j,k} v_i)) \\
&= -4\lambda \sum_j (S_{kj} - \lambda v_k v_j) v_j \\
&= -4\lambda (\sum_j S_{kj} v_j - \lambda v_k) = 0,
\end{aligned}$$

where we have used the symmetry of S_{ij} in the second step. Or,

$$Sv = \lambda v$$

The above eigenvector equation gives exactly N solutions. It shows us that the solution to the least square fit is given by an eigenvector of S_{ij}. By the finite dimensional spectral theorem, a Hermitian matrix S_{ij} can be decomposed as sums of outer products of its normalized eigenvectors weighted by the corresponding eigenvalues. Hence, the eigenvector with the largest eigenvalue would render the global minimum.

3.2 Curvature Measurement

As noted in section 3.1, the η-dependence in the definition of $\theta_\pm$ allows for an accurate measurement of the curvature using the theta-theta spectrum. The detailed procedure of such curvature measurement is presented in Baker et al. (2021, submitted) and Sprenger et al. (2021), which we briefly summarize here.

When we use a bad estimate of the curvature $\eta^* = k\eta$, $1 \neq k > 0$, in defining $\theta^*_\pm$, the resulting theta-theta spectrum is subject to a shearing. We can show that:

$$\theta^*_+ = \frac{1+k}{2k}\theta_+ + \frac{1-k}{2k}\theta_- \tag{3.14}$$

$$\theta^*_- = \frac{1-k}{2k}\theta_+ + \frac{1+k}{2k}\theta_- \ . \tag{3.15}$$

Under the above linear transformation, an arclet, instead of being mapped to the horizontal and vertical lines $\theta_\pm = \theta_j$, are now mapped to tilted lines. Examples of the theta-theta spectra generated with a good (left panel) and a bad (right panel) curvature estimate are presented in Figure 3.3. It is clear that the theta-theta spectrum is only well-modeled by an outer product if the curvature estimation is accurate enough.

We may generate a 1-parameter family of theta-theta spectra based on different curvatures used in evaluating $\theta_\pm$, and we can use the curvature that generated the theta-theta spectra with the largest eigenvalue as the best curvature estimation (Baker et al., 2021, submitted). The detailed procedure for estimating curvature, as outlined in Baker et al. (2021, submitted), is summarized below:

1. Fourier transform the dynamic spectrum to generate the secondary spectrum.
2. Determine the grid ($\theta_\pm$, curvature dependent) on which the $\theta - \theta$ spectra will be generated.
3. Given a curvature, create the theta-theta spectrum through the theta-theta mapping.
4. Calculate the largest eigenvalue for the resulting theta-theta spectrum.
5. Repeat steps 3 and 4 over a range of curvatures.
6. Fit a parabola to the peak of eigenvalue vs curvature.

The above procedure is applied to simulated data for a proof of concept. The result is shown in Figure 3.4.

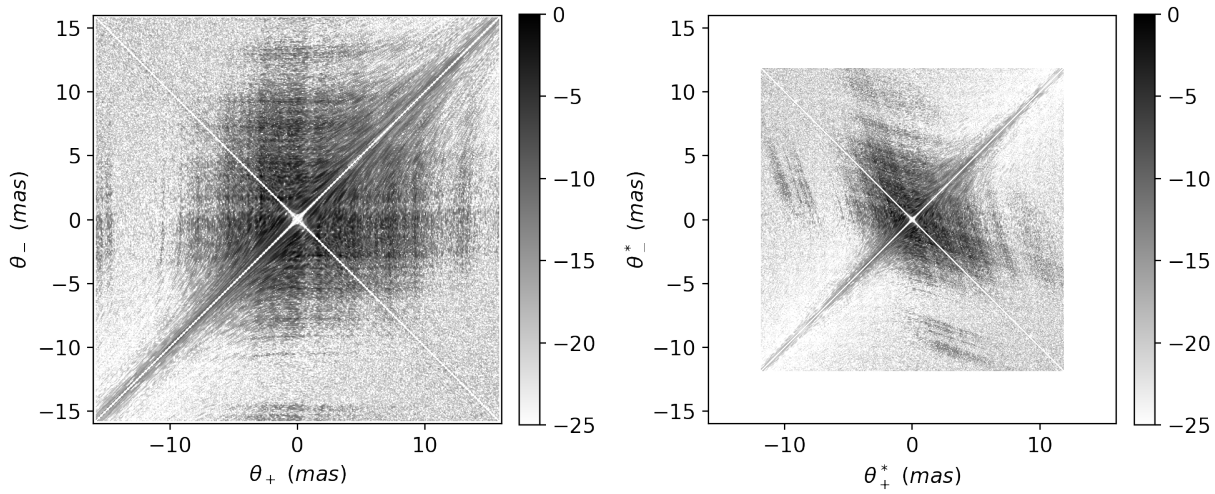

Figure 3.3: Examples of θ-θ spectra using good or bad curvature estimation. The first spectrum can be well-modeled by the outer product of its first eigenvector, whereas the second spectrum cannot be modeled well by any outer product.

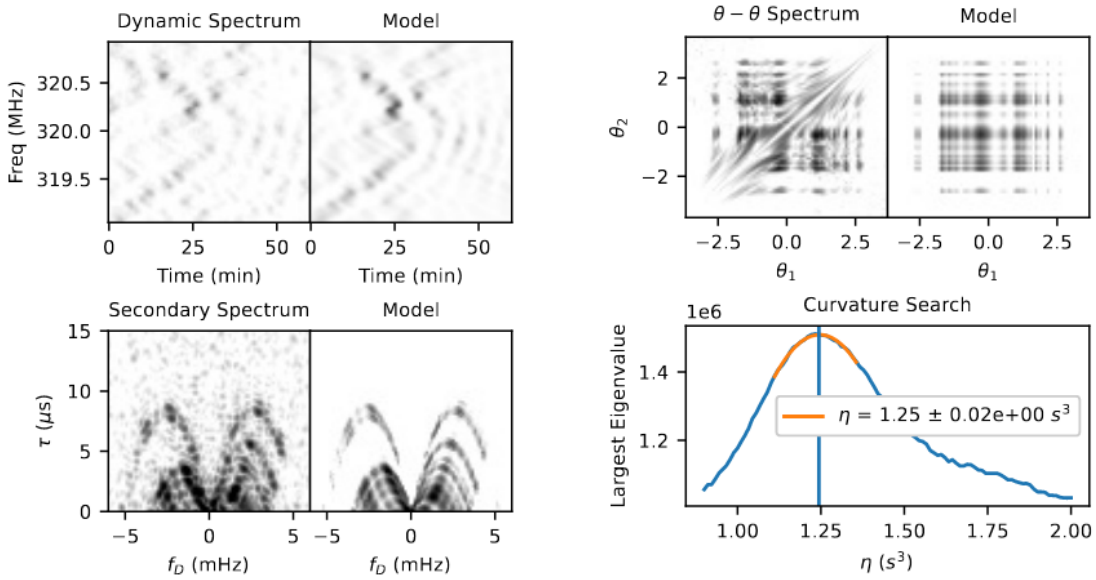

Figure 3.4: Example for the curvature search procedure applied to simulated data. Reprinted with permission from Baker et al. (2021, submitted). The plots include the data and models for dynamic spectrum, secondary spectrum, as well as theta-theta spectrum, where all models are generated using the best fit curvature. The lower right panel demonstrate the resulting eigenvalue as a function of curvature, which peaks at $\eta = 1.25(2)\ s^3$.

3.3 Phase Retrieval

Scattering by the interstellar medium can be well-characterized as a linear filter, or impulse response function. Hence, the observed signal is the convolution between the impulse response function of the ISM filter and the intrinsic pulsar signal (Walker et al., 2008; Walker & Stinebring, 2005; Walker et al., 2013; Pen et al., 2014). However, because the pulsar is intrinsically a white-noise generator, the observed electric field is an amplitude-modulated noise. So the signal contains no phase information, at least unless the periodicity of the signal is exploited through cyclic spectroscopy (Demorest, 2011). In other words, the impulse response function of ISM is not a direct observable. The observed signal can be written as the following:

$$E(t) = h(t) * E_0(t) \ , \tag{3.16}$$

where $h(t)$ is the impulse response function of the ISM screen, and $E_0(t)$ is the pulsar intrinsic spectrum.

We then Fourier transform the samples of the electric field during time $nT \leq t < (n+1)T$ to form a spectrum:

$$\begin{aligned} \hat{E}_n(\nu) &\equiv \int_{nT}^{(n+1)T} [h(t) * E_0(t)] \, \mathrm{e}^{-2\pi i \nu t} \mathrm{dt} \\ &= H_n(\nu) \hat{E}_0(\nu) \ , \end{aligned} \tag{3.17}$$

where $H_n(\nu)$ is the Fourier transform of $h(t)$ on the interval $nT \leq t < (n+1)T$, and $\hat{E}_0(\nu)$ is the Fourier transform of the intrinsic pulsar signal, which we assume to be stationary so independent of n. We may further stack such spectra together, and write:

$$\hat{E}(n, \nu) \equiv \hat{E}_n(\nu) = H(n, \nu) \hat{E}_0(\nu) \ , \tag{3.18}$$

where n is now denoting the time axis, following from the definition in Eqn 3.17. Recall that the phase of $E(n, \nu)$ is noise-like, as inherited from $E_0(t)$. Therefore, we take the squared modulus of $\hat{E}(n, \nu)$ and take its time-average on a small time scale ($\approx$ 10 s), much less than the characteristic time scale on which $H(n, \nu)$ varies ($\approx$ 5 min). The resulting spectrum is the dynamic spectrum, which can be written as:

$$\begin{aligned} I(t_k, \nu) \equiv \langle |\hat{E}(n, \nu)|^2 \rangle &= \frac{1}{N} \sum_{n=kN}^{(k+1)N} |H(n, \nu) \hat{E}_0(\nu)|^2 \\ &\approx |H(t_k, \nu)|^2 \cdot \langle |E(t)|^2 \rangle = |H(t_k, \nu)|^2 I_0 \ , \end{aligned} \tag{3.19}$$

where I_0 is the average intensity of the pulsar. Note that in deriving the above equation we assume the pulsar spectrum is flat, i.e. frequency independent, and we make the approximation that the impulse response function, $H(t_k, \nu)$, does not change in the time interval we are averaging over. For simplicity, we drop the subscript k in what follows.

The above calculation shows that the observed dynamic spectrum is the squared modulus of the impulse response function up to a scaling by the observed intensity of the pulsar. In other words, the amplitude of the impulse response function is given by the square root of the observed dynamic spectrum. The task of estimating the phase of $H(t, \nu)$ is known as the phase retrieval problem.

Following from Eqn 3.19, we define the conjugate spectrum as the following:

$$C(f_D, \tau) = \hat{I}(f_D, \tau) = I_0 \mathcal{F}\{|H(t, \nu)|^2\} = I_0 \cdot \mathrm{ACF}(h(f_D, \tau)) \ , \tag{3.20}$$

where $h(f_D, \tau)$, which we will refer to as the wavefield, is the Fourier transform of impulse response function $H(t, \nu)$, and ACF() denotes the auto-correlation of a signal. In the above derivation, we have used the Wiener-Khinchin theorem: the power spectrum of a function and the autocorrelation of that same function are a Fourier transform pair. Note that the secondary spectrum is defined to be the squared modulus of the conjugate spectrum, so all the mappings and methodologies introduced above regarding the secondary spectrum also apply to the conjugate spectrum, which is a complex Hermitian array. One distinction between the conjugate spectrum and the secondary spectrum is that the former carries phase information regarding the interference for a pair of scattered images, whereas the later only contains amplitude of the resulting interference.

It is clear that the conjugate spectrum is the auto-correlation of the wavefield, up to a scaling. Intuitively, in the regime of strong scattering, the wavefield contains only the interference information between the line-of-sight image with scattered images, which occupy a thin parabola if the scattering is highly anisotropic. It is the auto-correlation of the wavefield that produces the interference between all pairs of scattered images, which gives rise to the observed arclets in the secondary spectrum. A simulation justifying the above statement is given in Figure 3.5.

Although the phase-retrieval problem is in general ill-posed — namely infinitely many solutions exist — a reasonable estimate can be made in the highly anisotropic scattering scenario using the theta-theta mapping (Baker et al., 2021, submitted). The steps for the phase retrieval can be outlined as the following:

1. Determine the curvature of the scintillation arc.

2. Divide the dynamic spectrum into overlapping small chunks (This step effectively lowers the resolution of the conjugate spectra, and hence the theta-theta spectra, which makes the 1-d assumption more legitimate.)

3. Compute the (complex) theta-theta spectrum for each of the small chunks.

4. Calculate the (complex) eigenvector and eigenvalue of each theta-theta spectrum. Place the eigenvector along $\theta_- = 0$ in a theta-theta spectrum with zero everywhere else, and map it back to the conjugate spectrum as an estimate for the wavefield. (This is effectively placing the eigenvector along the parabola).

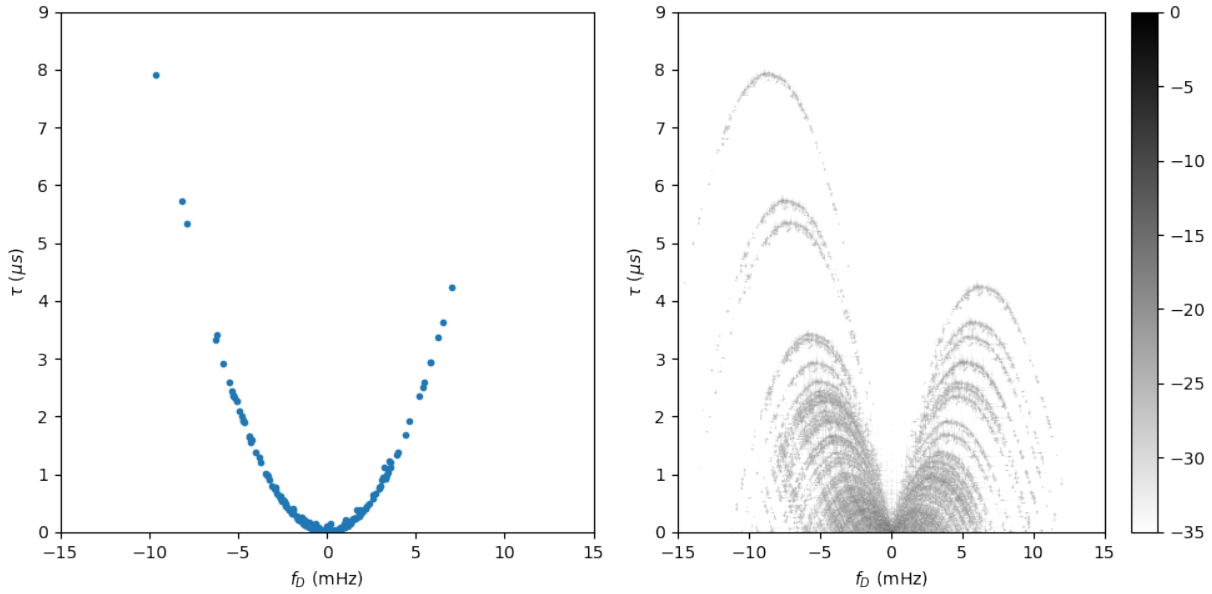

Figure 3.5: A simulation of a wavefield for a highly anisotropic scattering and its corresponding secondary spectrum. Each dot in the wavefield correspond to a scattered image by Eqn 2.8 and 2.9. The secondary spectrum is the auto-correlation of the wavefield, which gives rise to the arclets. Note that the apexes of the arclets correspond exactly to the scattered images in the wavefield.

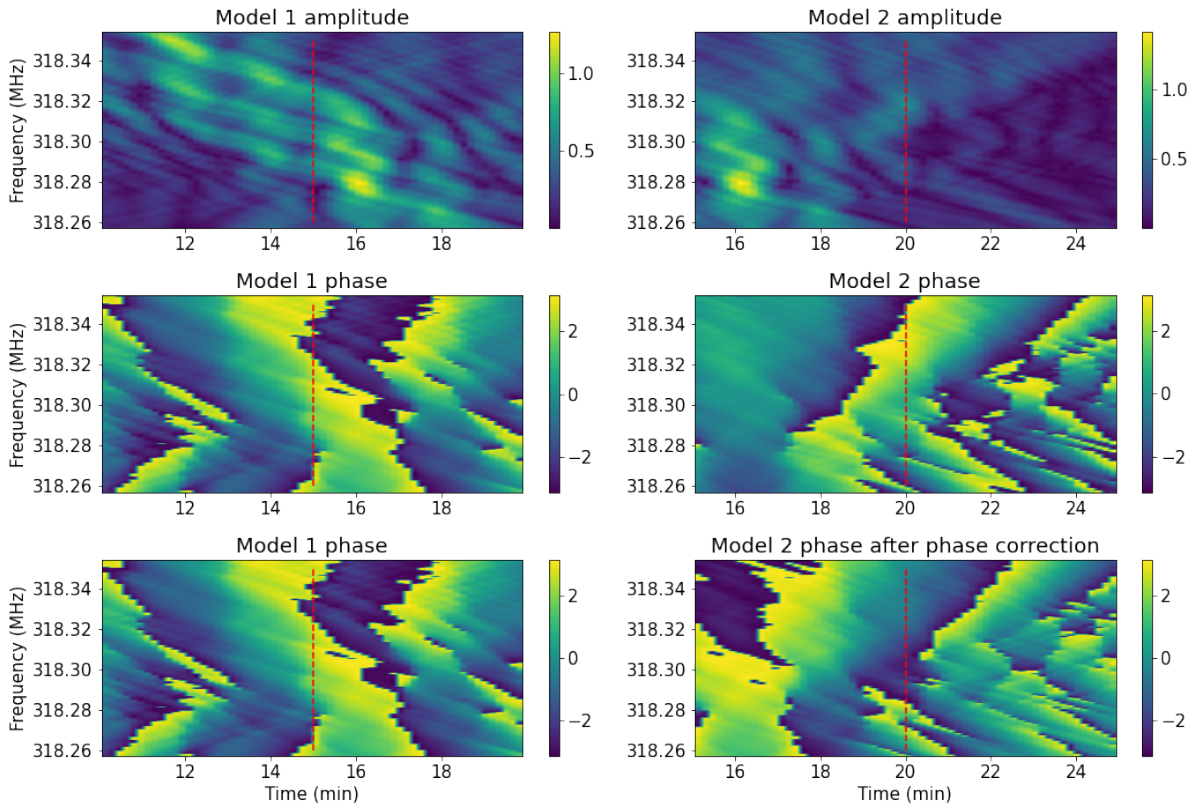

Figure 3.6: The amplitude and phase of the models for two overlapping chunks of a dynamic spectrum of B0834+06 on MJD 53665. The phase of the models, if the models were perfect, differs by a constant ϕ. The red dashed lines indicate the overlapping regions between the two models. The first and second rows show the amplitude and phase of the two models respectively. Though it seems that the phase from the two models disagree by a large amount in the middle left and middle right panel, the agreement between the phase is improved after correcting by the mean of the angle difference mod 2π.

5. Fourier transform the estimated wavefields into the time domain. We will obtain an estimation of the complex electric field for each small chunk of the data.

6. The phase of the models for two overlapping chunks differs up to a constant ϕ. We determine the relative phase rotation through the overlapping regions and correct for this rotation by multiplying $e^{-i\phi}$ to the model for the second chunks. See Figure 3.6 for an example.

7. Finally, we connect the models for different chunks together with their phase differences corrected. And, we replace the amplitude of the model with the square root of the amplitude of the dynamic spectrum. The resulting model is presented as an estimation of the impulse response function.

The above procedure essentially deconvolves the conjugate spectrum with the best model assuming the

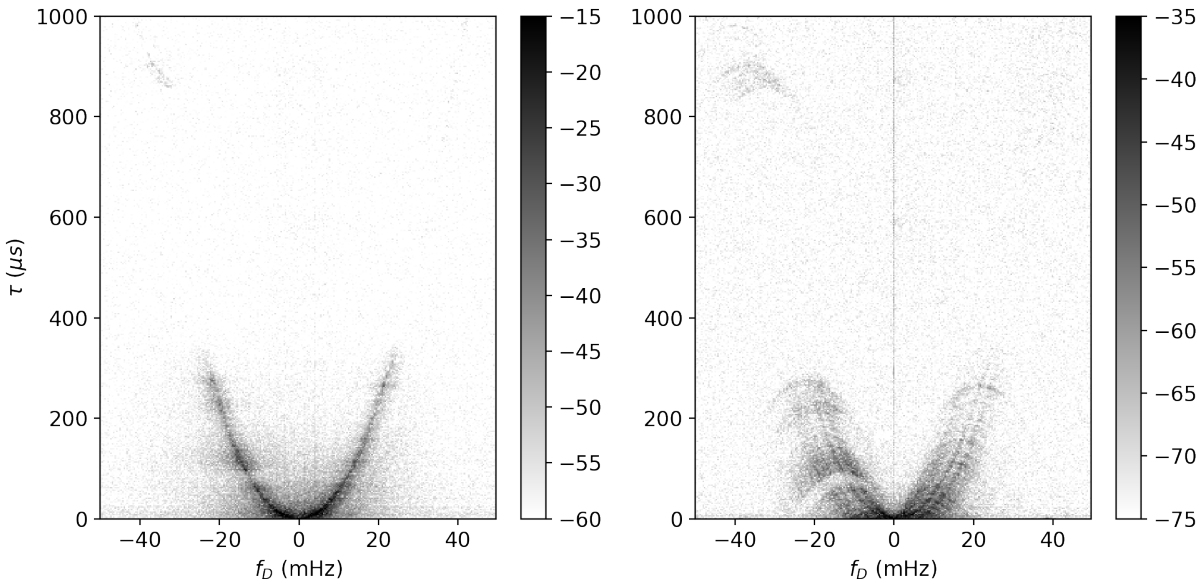

Figure 3.7: The estimated wavefield using the theta-theta method and its corresponding secondary spectrum.

scattering is linear. This method may also apply to double screen scattering, given that the power from the second screen is well separated from that of the dominating screen in the secondary spectrum (Baker et al., 2021, submitted). An example of an estimated wavefield from the above procedure is presented in Figure 3.7.

3.4 Sky Mapping

The wavefield contains information regarding the interference of the electric field from all scattered images with the line-of-sight image alone, which means that, assuming a single screen, we can reconstruct the image of the pulsar with two-fold degeneracy based on Eqn 2.8 and 2.9. Let positive x be the direction of the effective velocity, and y be perpendicular to it. We can write the angular position of a scattered image with respect to the line-of-sight image to be (θ_x, θ_y). This implies that:

$$f_{Dj} = -\frac{V_{\text{eff}}\theta_x}{\lambda} \tag{3.21}$$

$$\text{and } \tau_j = \frac{D_{\text{eff}}(\theta_x^2 + \theta_y^2)}{2c} \ . \tag{3.22}$$

Note that a constant f_{Dj} constrains the θ_x component for a scattered image onto a line perpendicular to the angular velocity, whereas a constant τ constrains a scattered image to lie on a circle centered on the line-of-sight image with radius $2c\tau_j/D_{\text{eff}}$. Hence, given the Doppler frequency and the delay corresponding to a scattered image, the image is constrained onto the intersection(s) between the line and the circle (see Figure 3.8).

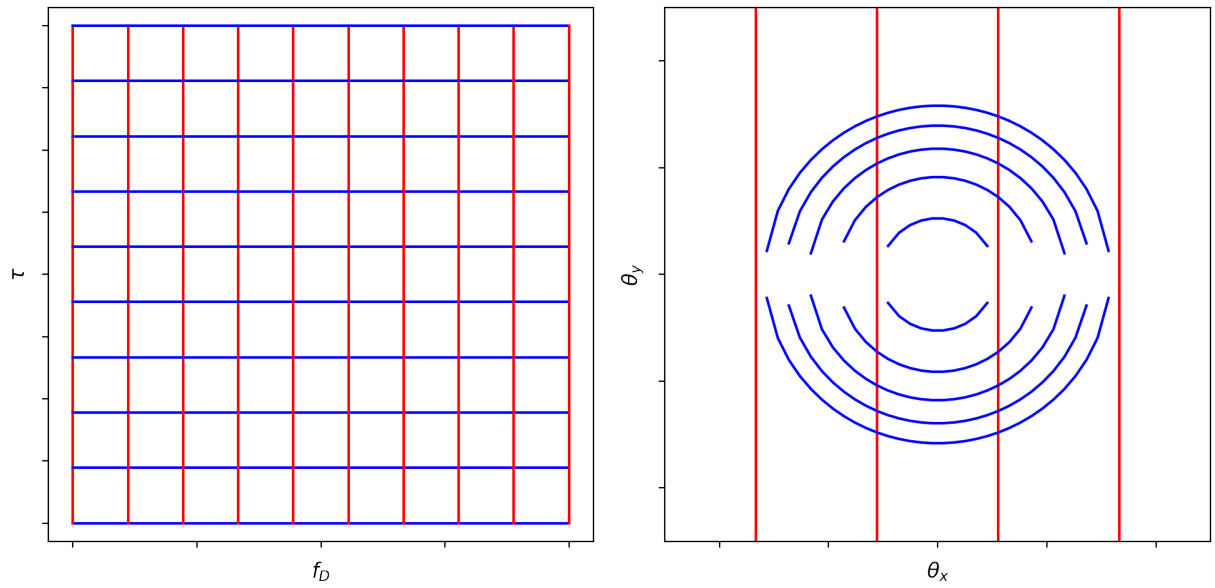

Figure 3.8: Lines with constant delay and Doppler frequency under the Sky mapping. Different from the theta-theta mapping (Figure 3.1), constant delays are mapped to circles, whereas constant Doppler shifts are mapped to straight lines parallel to the y axis.

Solving for θ_x and θ_y from the above equations further yields

$$\theta_x = -\frac{\lambda f_{Dj}}{V_{\rm eff}} \ , \tag{3.23}$$

$$\text{and } \theta_y = \pm\sqrt{\frac{2c\tau_j}{D_{\rm eff}} - \theta_x^2} \ , \tag{3.24}$$

where α is given by $\alpha = \arctan\{\theta_y/\theta_x\}$. We can then map the wavefield through a coordinate transform from (f_D, τ) to (θ_x, θ_y):

$$I(\theta_x, \theta_y) \equiv h(f_D(\theta_x, \theta_y), \tau(\theta_x, \theta_y)) \left| \frac{V_{\rm eff} D_{\rm eff} \theta_y}{c\lambda} \right| , \tag{3.25}$$

where the last term is the determinant of the Jacobian for the transformation, included for flux preservation. A result of such mapping is presented in Figure 3.9. Note that to calculate the above sky image, we need both the effective velocity of the scintillation pattern and the effective screen distance, as defined in Eqn 2.4 and 2.7 respectively.

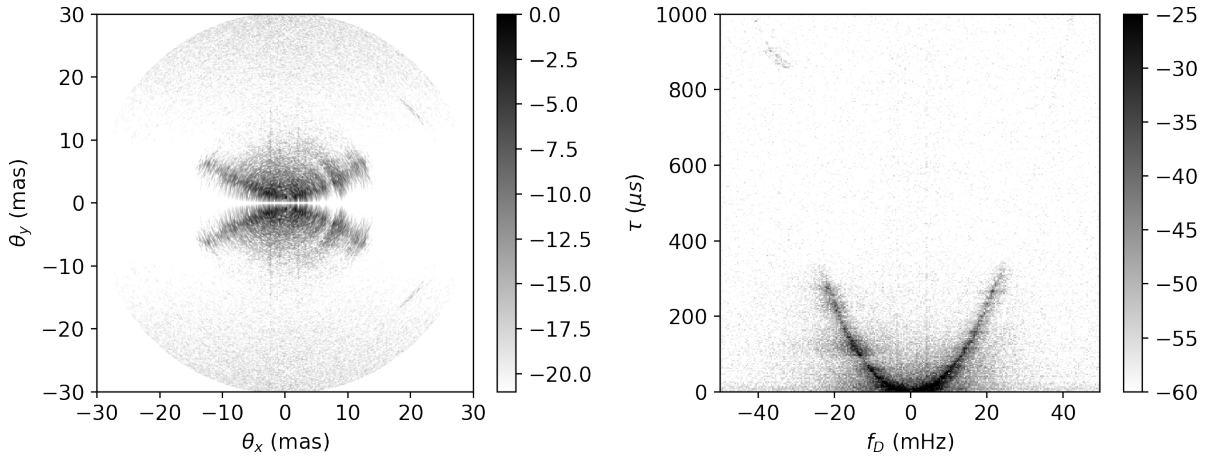

Figure 3.9: The estimated wavefield (left) and the resulting image of the pulsar using the mapping defined in Eqn 3.25 (right). Observe that the image is symmetric about the x axis, corresponding to the two-fold degeneracy in determining the angular position of a scattered image from the Doppler frequency and delay relative to the line-of-sight image. The screen distance and effective velocity used in the mapping is reported in Brisken et al. (2010) based on VLBI observations.

Chapter 4

Report of a spectacular double-lensing event of PSR B0834+06

4.1 Observation Summary

We report on an archived 7-epoch observation of the pulsar PSR B0834+06, observed at the Arecibo Observatory from 2005 October to December with weekly cadence. We obtained dynamic spectra of duration 45 minutes using the 327 MHz receiver with spectral resolution of approximately 0.38 kHz/channel centered at 318.5 MHz. The 2048 frequency channels yields a total bandwidth of 0.78 MHz. We used an integration time of 10s, so there are 270 time bins per dynamic spectrum. The frequency and time resolution yield Nyquist rates of 1.3 ms in delay and 50 mHz in Doppler frequency, which sufficiently contain all scintillation signatures. Scintillation arcs were consistently found in all secondary spectra with rich arclet structures, which implies a highly anisotropic scattering scenario (Walker et al., 2004).

We present the the seven dynamic spectra and their corresponding secondary spectrum in Figures 4.1–4.7. Note in particular the feature at approximately 1200 μs and -40 mHz in the secondary spectrum on MJD 53665. We refer to it as the 1 ms feature. The feature has drifted down in delay over time: on MJD 53712, its delay decreases to 700 μs. The motion of this feature in the secondary spectrum is a result of the relative motion between the pulsar, lens, and observer during a course of approximately 50 days.

In this chapter, we will present evidence that the 1 ms feature arises from doubly refracted rays by a dominant scattering screen, which also gives rise to the main scintillation arcs, and an isolated, elongated lens lying between the screen and the pulsar. The isolated lens has an aspect ratio of $\gtrsim 8.5$ and remains essentially stationary. Through the deflection angle by this isolated lens, we estimate the lower bound for the integrated column electron density within the lens, assuming it is perpendicular to the line-of-sight. Such a lens can potentially cause an Extreme Scattering Event. This is the central result of the thesis.

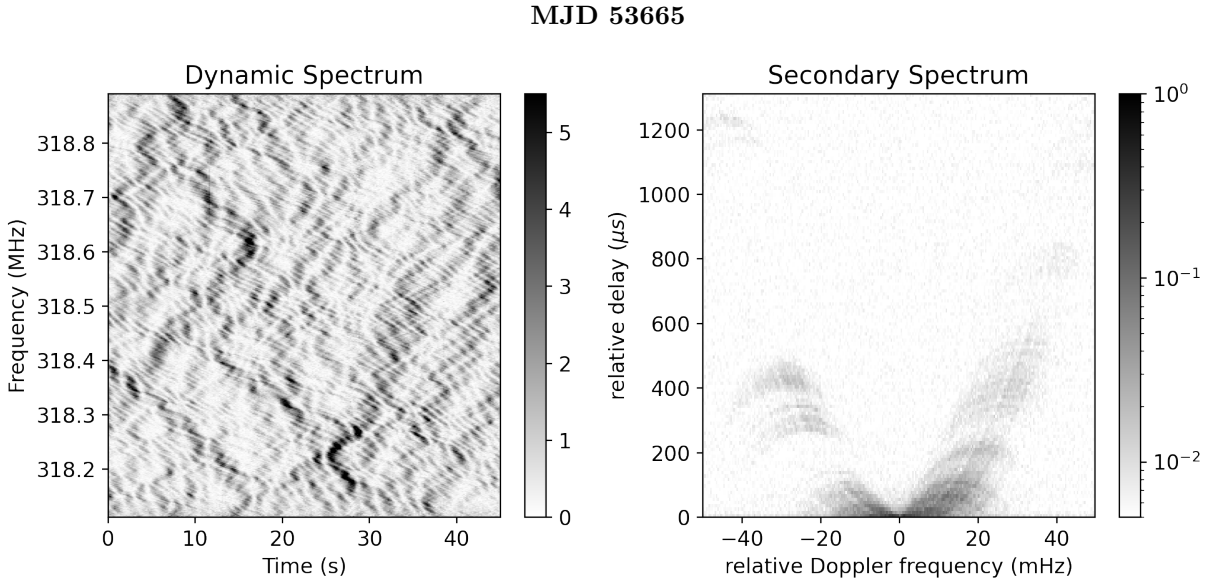

Figure 4.1: Dynamic and secondary spectrum of B0834+06 on MJD 53665, or 2005 October 22$^{\text{nd}}$.

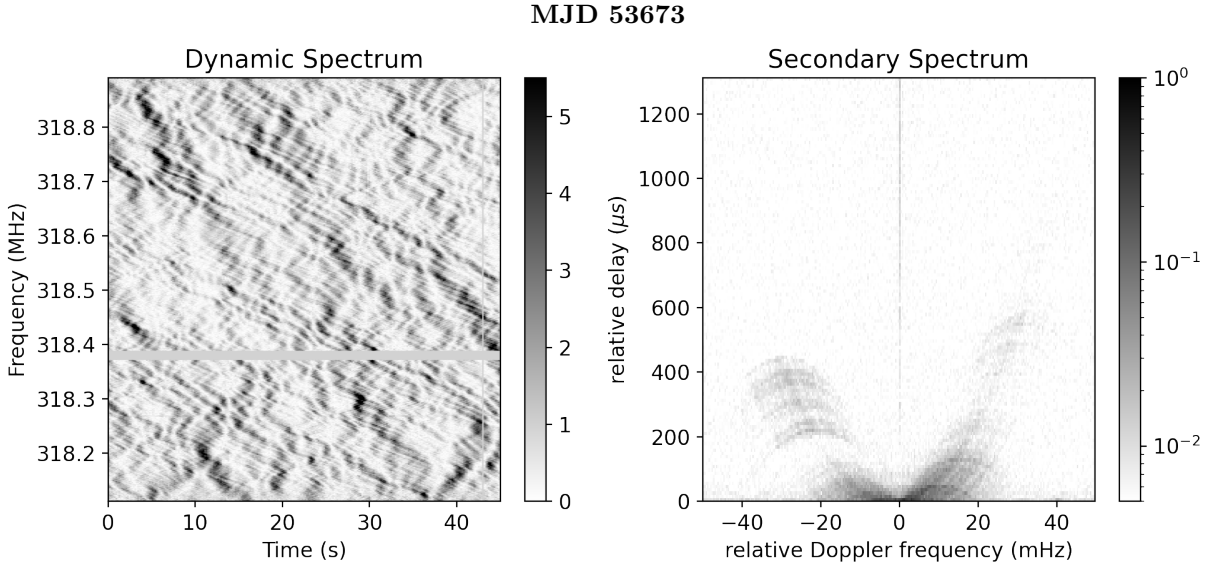

Figure 4.2: Dynamic and secondary spectrum of B0834+06 on MJD 53673. The 1 ms feature is not visible during this epoch; we do not yet have a satisfactory explanation for this absence.

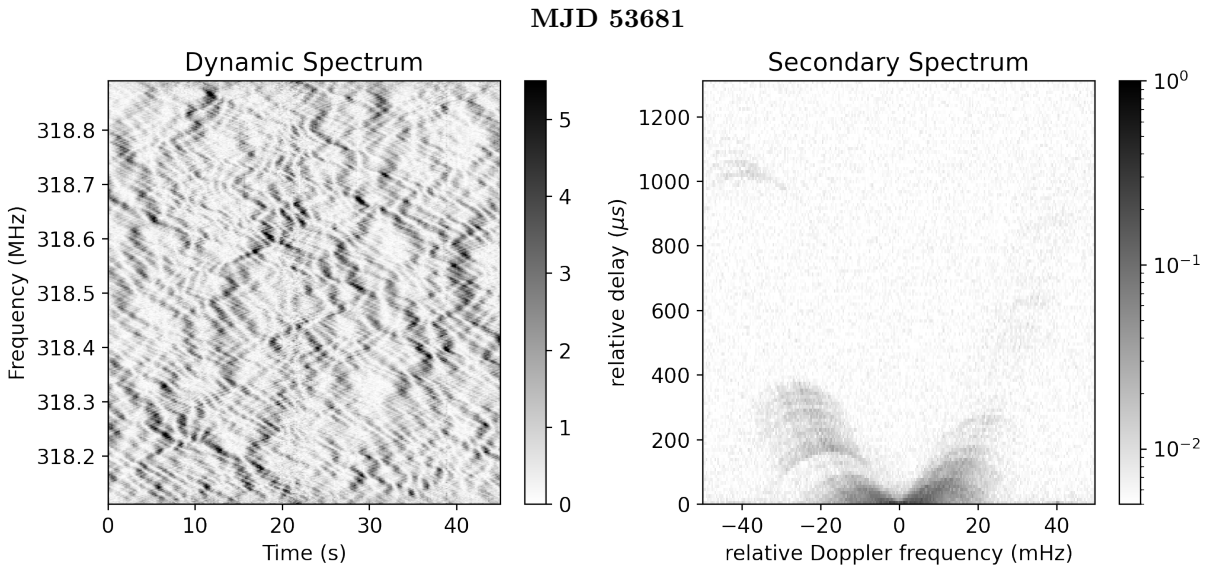

Figure 4.3: Dynamic and secondary spectrum of B0834+06 on MJD 53681.

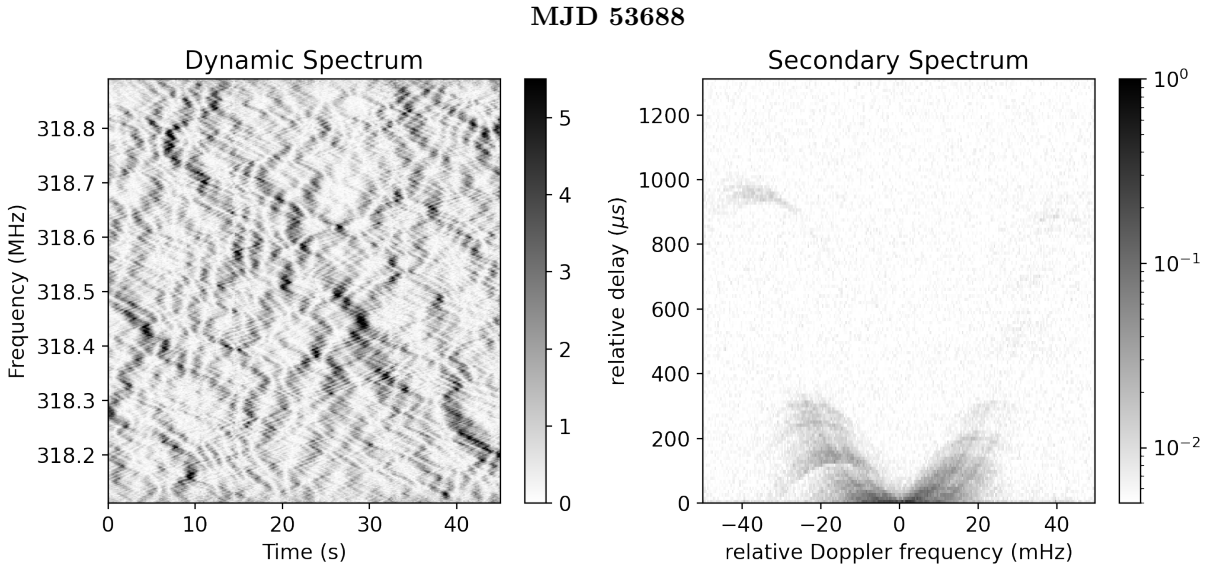

Figure 4.4: Dynamic and secondary spectrum of B0834+06 on MJD 53688.

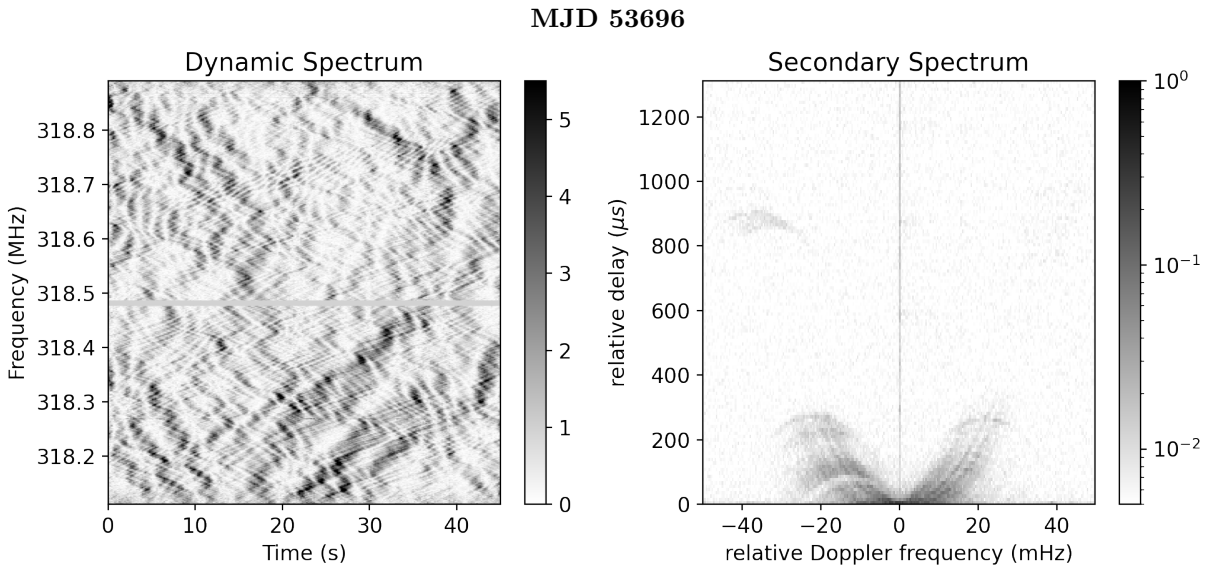

Figure 4.5: Dynamic and secondary spectrum of B0834+06 on MJD 53696.

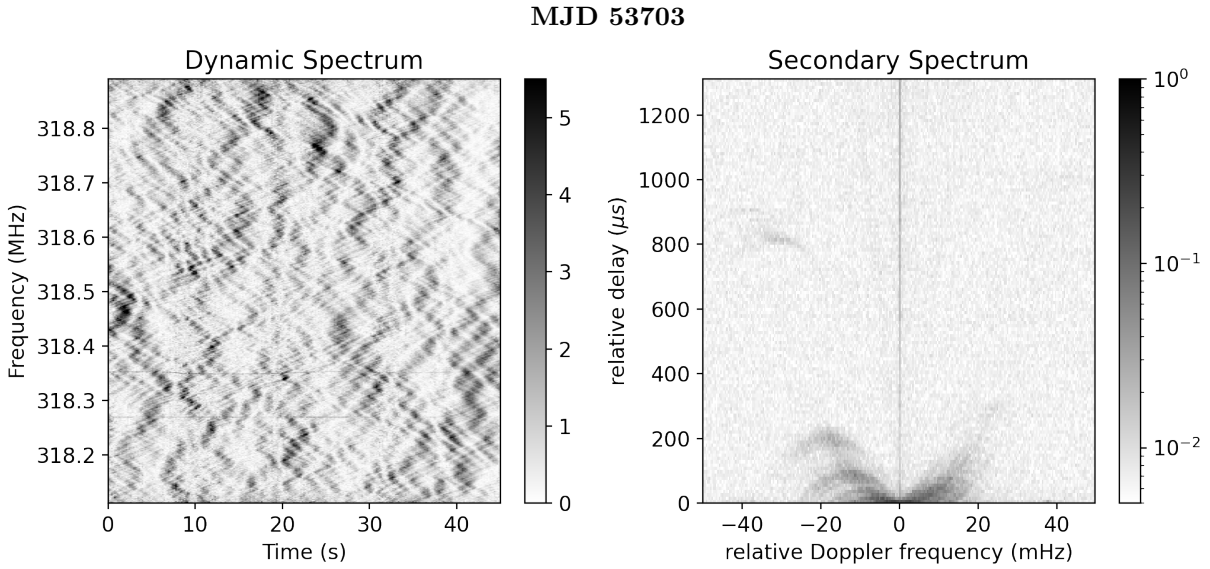

Figure 4.6: Dynamic and secondary spectrum of B0834+06 on MJD 53703.

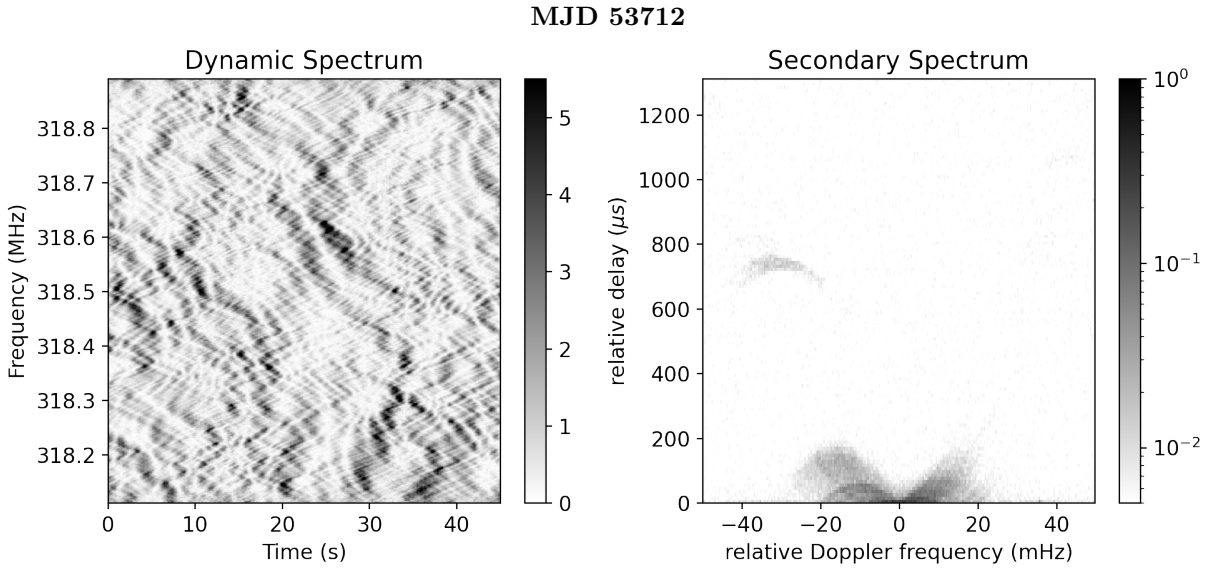

Figure 4.7: Dynamic and secondary spectrum of B0834+06 on MJD 53712.

4.2 Summary of Previous Work

Coincidentally, an VLBI observation of the same source was conducted on 2005 November 12, during our seven observation epochs (Brisken et al., 2010; Liu et al., 2016; Baker et al., 2021, submitted; Simard et al., 2019). They confirm that, overall, the scattered image of the pulsar is highly anisotropic. The 1 ms feature lies slightly inward of the main parabolic arc in the secondary spectrum and has a distinct VLBI signature. Hence, in Brisken et al. (2010) they conclude that the 1 ms feature is associated with a second lens, lying almost parallel with the pulsar images scattered by the dominant screen. For simplicity, we hereby refer to the dominant screen as screen 1 and the isolated lens, giving rise to the 1 ms feature, as screen 2. It was later proposed that the 1 ms feature actually arises from double lensing by screen 1 and screen 2 in Liu et al. (2016).

Through the single epoch VLBI observation, the effective distances (Eqn 2.7) for both scatterers and the effective velocity (Eqn 2.4) are accurately measured. We use the parameters reported in Liu et al. (2016) and Brisken et al. (2010) in our following analysis. The parameters for the two screens are summarized in Table 4.1.

The reconstructed image of B0834+06 from Brisken et al. (2010) is shown in Figure 4.8. The x and y axis are the relative right ascension (α or east-west) and relative declination (δ or north-south). The line-of-sight image is at (0, 0), and each red dot represents the apex of an arclet. The two groups of linear images, well-separated from the main image, are candidates for the sky location associated to the 1 ms feature. They later conclude that the 1 ms feature corresponds to the lower right group of images. The velocity of the pulsar is almost due north, indicated by the red arrow.

Table 4.1: Screen parameters reported in Brisken et al. (2010) and Liu et al. (2016). The first five quantities are directly measured through VLBI; the pulsar distance ($D_{\rm psr}$) and the pulsar angular velocity in the east and north directions, (μ_α and μ_δ), are estimated by model fitting; the rest are calculated based on the above pulsar velocity of and distance. The uncertainties do not contain the uncertainties in the pulsar distance and velocity. $D_{1\rm eff}$ and $D_{2\rm eff}$ are the effective distance to screen 1 and screen 2 respectively, and D_1 and D_2 are the physical distance between the screens and the observer. All parallel signs means the component of the vectors projected to the orientation of the linear images, whereas perpendicular signs means the component perpendicular to it.

Parameters	**Values**
$D_{1\rm eff}$	1044 ± 22 pc
$D_{2\rm eff}$	1252 ± 49 pc
$V_{\rm eff\parallel}$	305 ± 3 km/s
$V_{\rm eff\perp}$	-145 ± 9 km/s
$\parallel$ Scattering axis	-25.2 ± 0.5 deg east of north
$\perp$ Scattering axis	-115.2 ± 0.5 deg east of north
$D_{\rm psr}$	620 ± 60 pc
μ_α	2.16 ± 0.19 mas/yr
μ_δ	51.64 ± 0.13 mas/yr
D_1	389 ± 5 pc
D_2	415 ± 11 pc
$V_{\rm scr\parallel}$	-16 ± 10 km/s
α	27 ± 2 deg.

However, our analysis has shown that the reconstructed sky image (Figure 4.8) in Brisken et al. (2010) is subject to a sign flip. (We have been in touch with Dr. Brisken about this, and he agrees that our analysis is valid.) As in Figure 4.8, when the pulsar moves, both groups of images corresponding to the 1 ms feature move away from the pulsar, which indicates that the 1 ms feature increases in delay with time. This contradicts our 7 epoch observations, as presented in Figure 4.1-4.7. Also, as the 1 ms feature has negative Doppler frequency, we know that $\boldsymbol{V}_{\rm eff} \cdot \boldsymbol{\theta}$ must be positive from Eqn 2.8, or the angular separation between the scattered image and the pulsar image and the effective velocity must be on the same side of the line-of-sight image. Some more careful analysis regarding the curvature shows that both of the axes should be flipped in Fig 4.8, except for the pulsar velocity.

In the following sections, we test the above geometry by studying the temporal evolution of the 1 ms feature using the novel theta-theta methods introduced in Chapter 3.

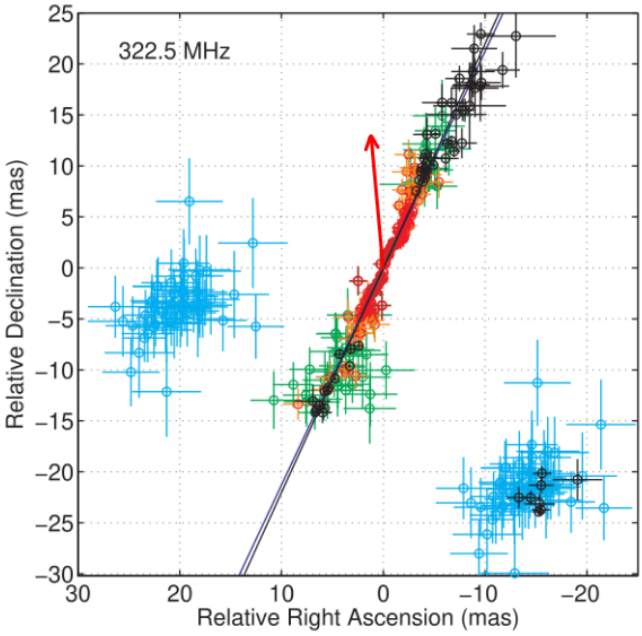

Figure 4.8: Map of the astrometric positions of the scattered radiation: Figure 2 in Brisken et al. (2010). We note that all the images should be flipped about the origin.

4.3 Evolution of the Double Lensing Event

4.3.1 Secondary spectra and curvature measurement

To better see the evolution of the features across the seven secondary spectra, we plot them side by side in Figure 4.9. For each secondary spectrum, we estimate the curvature for the bottom part of the scintillation arc ($\leq 500\mu s$) using the theta-theta mapping as described in section 3.2. Parabolas with the measured curvatures are overplotted in the secondary spectra. It is clear that the 1 ms feature consistently lies slightly inside the best fit parabolas, which, combined with the VLBI result, indicates the existence of a second scattering screen.

The measured curvature versus observation date for a year-long observation campaign is presented in Figure 4.10. The seven observations that we are analyzing here are highlighted in orange. Note that there are several measurements of the curvature for any single day as we observed the pulsar at multiple frequencies simultaneously.

Based on the pulsar and screen parameters in Table 4.1 and the known Earth motion, we can also predict the temporal variation based on Eqn 2.12, which repeated here:

$$\eta = \frac{D_{\rm eff}\lambda^2}{2cV_{\rm eff\|}^2} \ . \tag{4.1}$$

The result is overplotted with the measured curvature as the black curve in Figure 4.10. Overall, we

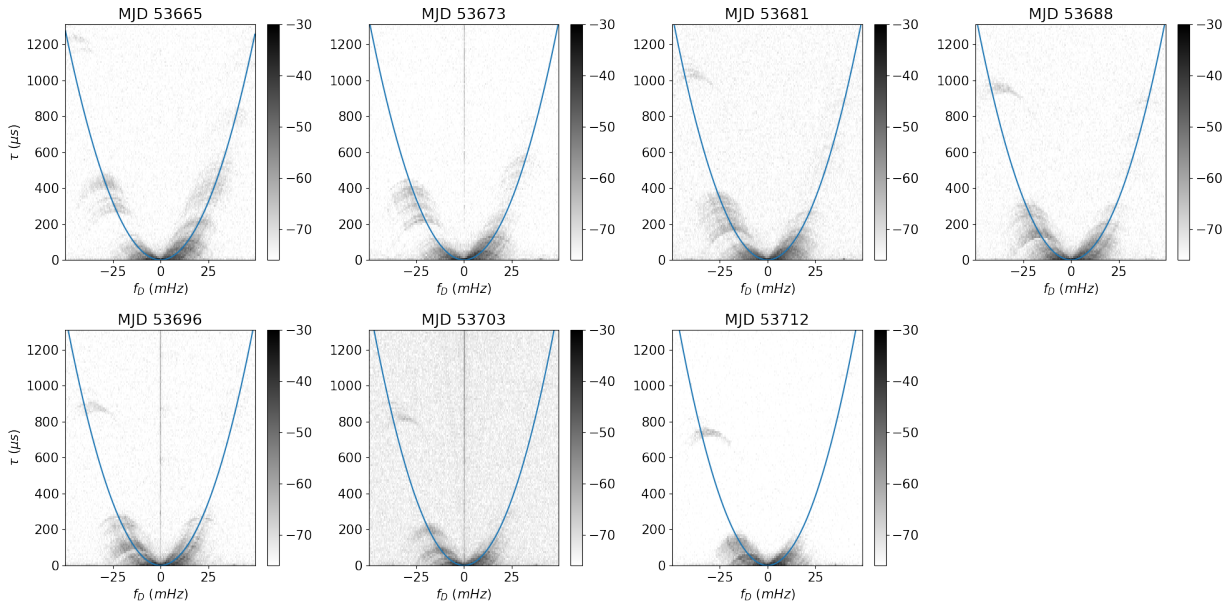

Figure 4.9: Temporal evolution of the secondary spectra. Pay special attention to the motion of the 1 ms feature. A parabola is plotted with the best fit curvature using the method described in section 3.2. It is clear, with the parabola plotted, that the 1 ms feature does not lie on the main scintillation arc.

find that the model yields a curvature that is about 2 sigma away from the measured values. To correct for the inconsistency, we conducted a single-parameter fit of the screen velocity, $V_{\mathrm{scr}\parallel}$ as in Table 4.1, which is the worst-constrained parameter. The best fit screen velocity is $-19.7(5)$ km/s, and the resulting model is plotted as the blue curve in Figure 4.10. The two red curves indicate the uncertainties in the measured screen velocity. We find a χ^2_r of 3.1 for the best fit model; this is due to the unreliable error bars for some outliers.

4.3.2 Theta-theta spectra and 1-D brightness distribution

We then calculate the theta-theta spectra for all seven observations based on the curvature measurement (Figure 4.11).

Note that the power in the theta-theta spectra does not occupy the entire square region. This is because the Nyquist rate in delay and Doppler frequency are mapped to hyperbolas and straight lines, respectively, by the theta-theta transform. Note that the 1 ms feature is now tilted and curved in all the theta-theta spectra, whereas the other features remain horizontal and vertical. This further indicates that the feature does not lie along the main scintillation arc.

We further calculate the eigenvector, or best fit 1-D brightness function, from each observation. The resulting brightness functions are plotted in Figure 4.12. The intensity for the brightness functions is pre-

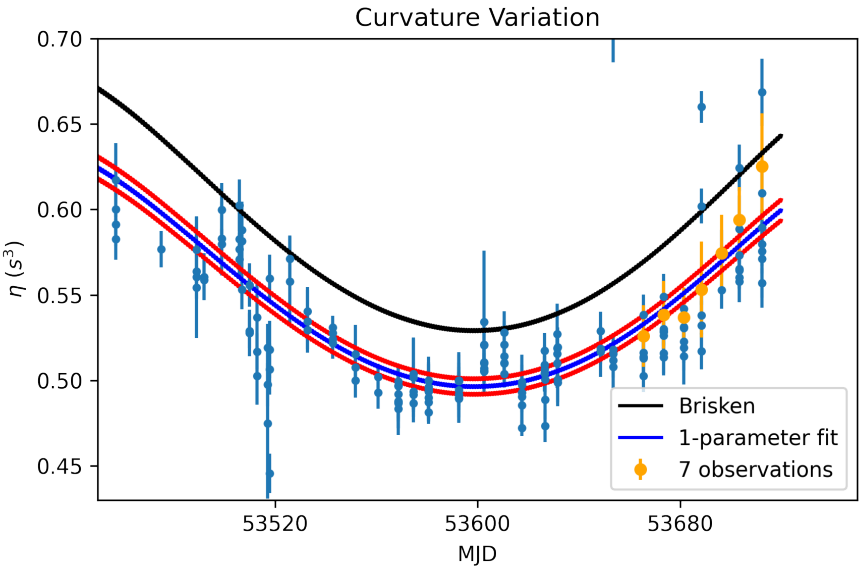

Figure 4.10: Curvature evolution during the 7 epochs and for 50 epochs prior to that date. (Observations from Stinebring et al., private communication.)

sented using a log scale, and the maximum for each brightness function are aligned with the observation date. We find that the peaks, or scattered images, move at an almost constant velocity as the pulsar moves. The 1 ms feature is manifested as the peak at around -20 mas.

4.3.3 Phase retrieval and wavefields

We then estimate the wavefield for each observation based on the phase retrieval technique introduced in section 3.3. Although the pulsar is scattered by two screens, the phase retrieval based on the theta-theta mapping still yields reasonable results for the following reasons:

1. The scattering is dominated by screen 1.
2. The signature from screen 2 is well-separated[1] from that of screen 1 in the secondary spectrum.
3. The scattered image by screen 1 is known to be essentially linear (Figure 4.8).

The resulting wavefield spectra are presented in Figure 4.13. Recall that all cross interference between two scattered images disappears in the wavefield; only signatures from scattered images interfering directly with the line-of-sight image are left, which correspond to the apexes of arclets.

[1] We only model the bottom portion of the scintillation arc ($\tau \leq 500\mu s$) in the phase retrieval.

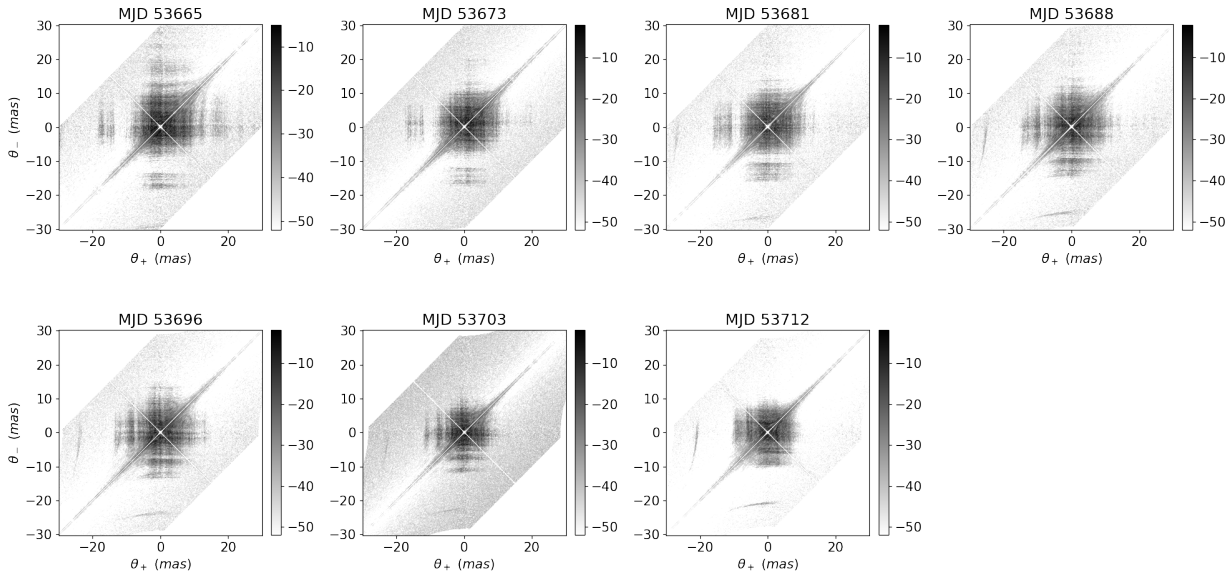

Figure 4.11: Temporal evolution (in the theta-theta spectrum) of the 1 ms feature reported in (Brisken et al., 2010). The 1 ms feature manifests as the tilted linear structure at around $\theta\pm = -25mas$.

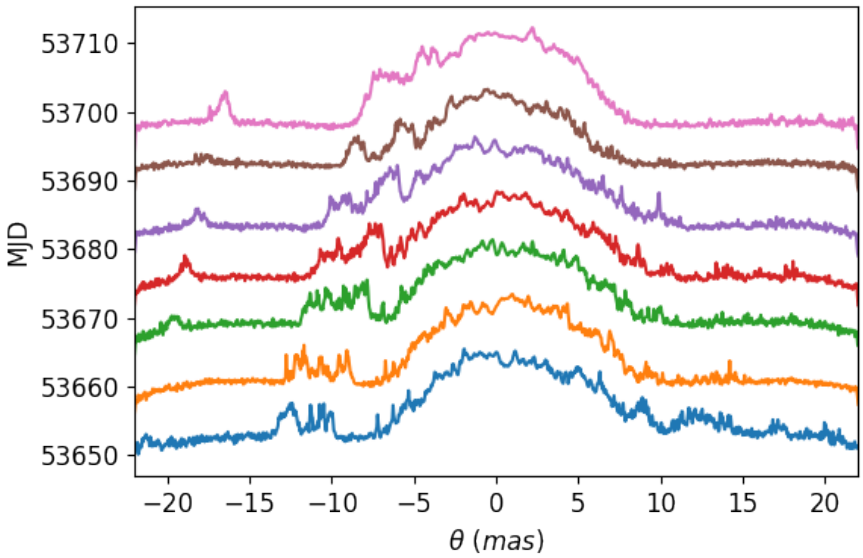

Figure 4.12: 1d brightness evolution.

4.3.4 Sky images

Recall, from section 4.3.4, that the wavefield can be mapped to a sky image with a two-fold degeneracy, namely symmetry about the effective velocity vector. Note that the only assumption for such mapping

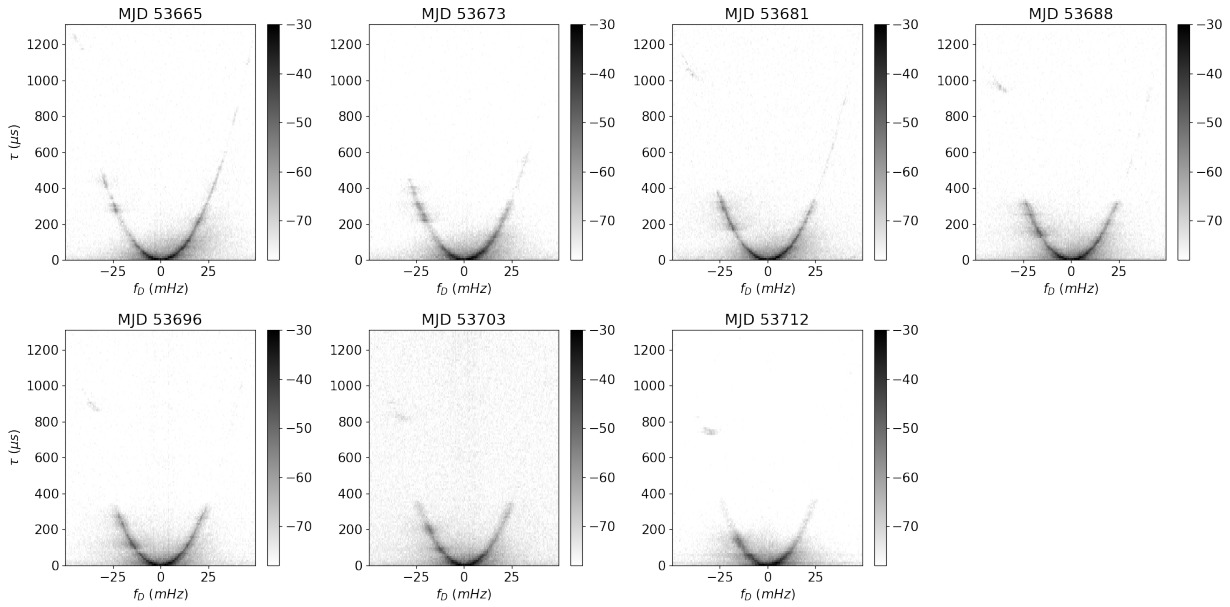

Figure 4.13: Temporal evolution of the wavefield.

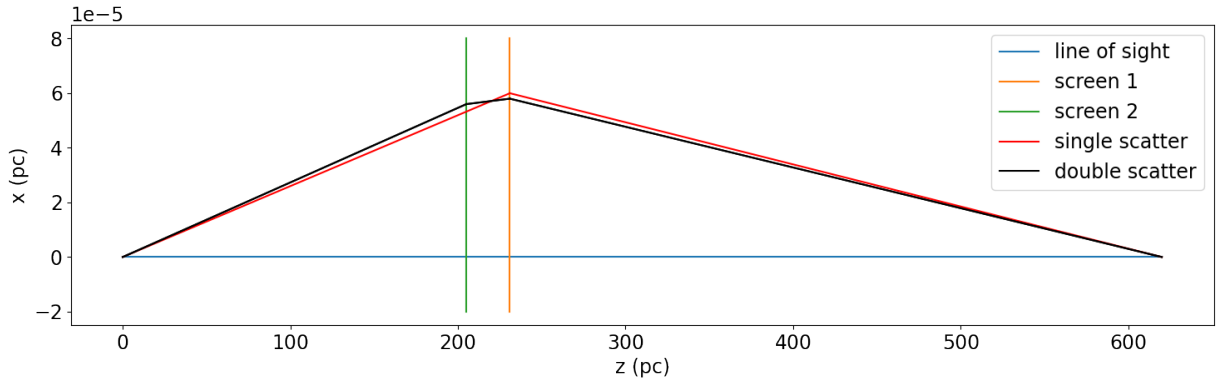

Figure 4.14: Comparison between rays scattered by one or both screens. The pulsar is on the left and the observer is on the right. Note the large difference in transverse and longitudinal scales.

is single screen scattering; specifically, the scattered images do not need to be linear for such mapping to produce an accurate result.

However, one complication arises when applying such mapping to the seven observations: the rays from the 1 ms feature are scattered by two screens and hence strictly violate the assumption. However, since the distance between the two screens (25 pc) is small compared to the distance between Earth and the pulsar (620 pc), the sky mapping remains reasonably accurate for the 1 ms feature. To demonstrate this, we compare a ray only scattered by screen 1 and a ray scatted by both screens with the same length in Figure

4.14. The resulting angular difference between the rays' intersection with screen 1 is about 1 mas when the corresponding scattered image is separated from the line-of-sight image by 32 mas. Note that in the plot, the scale for the x axis is magnified by a factor of 10^5.

Assuming all scattering occurs at the distance of screen 1, we present the sky images inferred from the wavefield in Figure 4.15. Recall that the θ_x axis in the sky images corresponds to the direction of the effective velocity. As the system evolves, the 1 ms feature gradually decreases in θ_x.

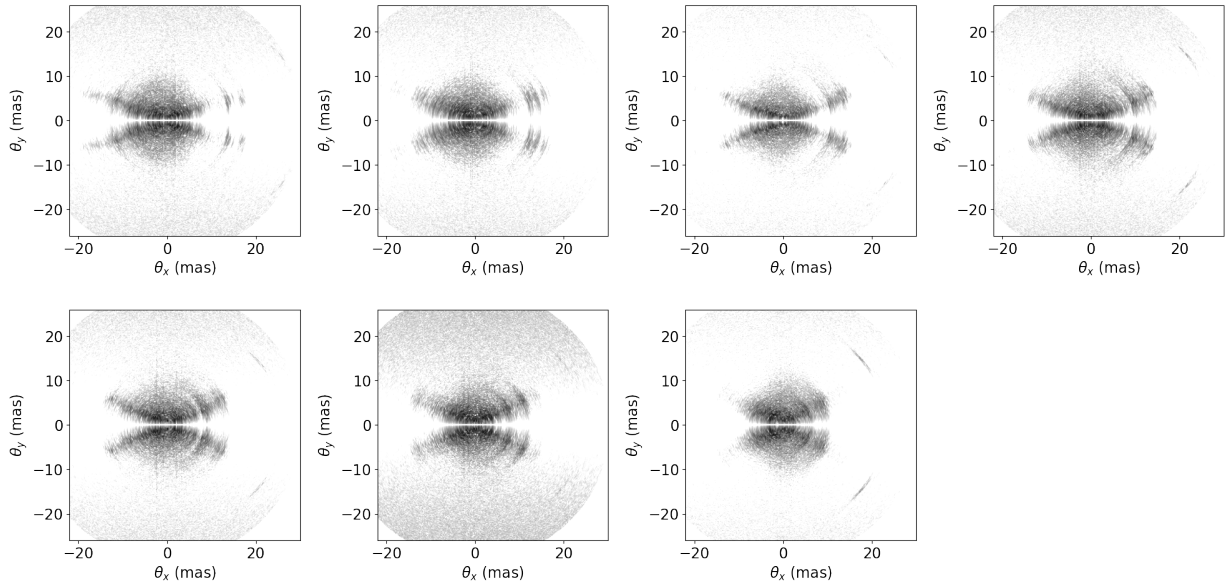

Figure 4.15: Evolution of the sky images inferred from the wavefield. The image is symmetric about the θ_x axis.

Note that the 1 ms feature is mapped to a straight line. This indicates a high aspect ratio for the lens on screen 2 causing the 1 ms feature. However, we note that the images seem to be blurred into arc-like structures centering the origin. This blurring is caused by the pixel shape in the delay axis. Namely a constant delay constrains the image to a circle. To rule out that the highly anisotropic images at the 1 ms feature is caused by some mapping artifacts, we also identify bright images from the wavefield directly by eye and perform discrete mappings. An example of the identified bright images is given in Figure 4.16. The discrete imaging of the 1 ms feature from all epoch is plotted in Figure 4.17. The left panel assumes that the pulsar is always at the origin for all the epochs, whereas the right panel moves the pulsar by the known effective motion. We see that, after correcting for the pulsar's apparent location, the discrete images of the 1 ms feature from different dates line up perfectly. We further estimate a lower bound for the aspect ratio of the lens by comparing the standard deviation of images location along the lens and those across the lens. The lower bound for the aspect ratio is about 8.5(8): the length of the lens divided by the width of the lens.

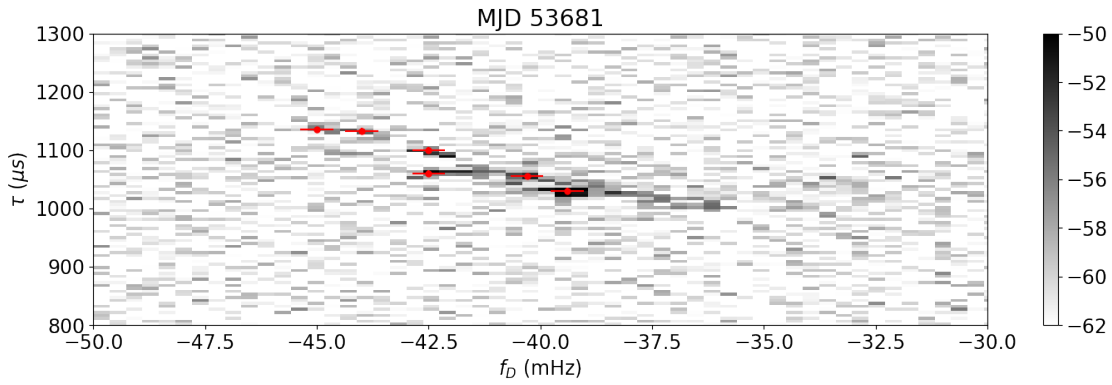

Figure 4.16: Evolution of the sky images inferred from the wavefield. The image is symmetric about the θ_x axis.

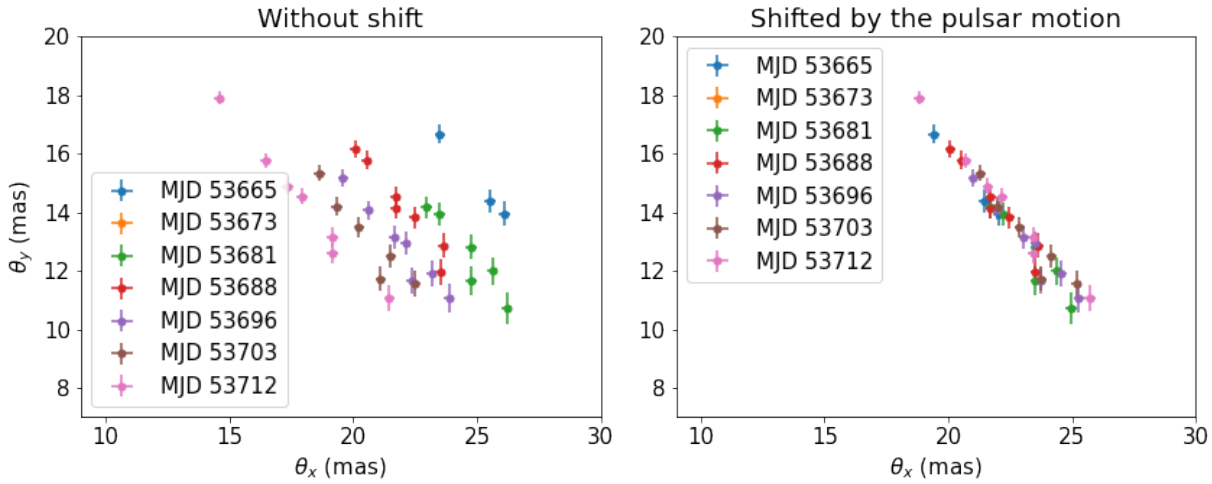

Figure 4.17: The discrete image of the 1 ms feature by identifying bright pixels (images) in the wavefield. The left panel assumes that the pulsar is always at the origin for all the epochs, whereas the right panel shifts the pulsar by the known effective motion.

4.4 Scattering by Multiple Linear Lenses

In a model independent way, we have shown that the 1 ms feature comes from double lensing by essentially a linear lens at screen 2 and a set of linear lenses at screen 1. To further explore the scattering geometry, we need to introduce some theory regarding lensing by two linear lenses.

One key property of refraction by a linear lens is that the lens only deflects the ray in a perpendicular direction. To better visualize this, we present the geometry of a refracted ray by a linear lens in Figure 4.18. The linear lens is extended along the x axis. The incident ray is in orange and the refracted ray is in red. We

draw the projection of this geometry onto the plane $y = 0$ (left) and $x = 0$ (right). Note that the direction of the ray does not change in the x direction, but the ray is deflected with an angle α in the y direction. This is because the lens has uniform electron density along the x axis, which implies a constant index of refraction. A change in the index of refraction is required to deflect a ray, so there must be a gradient in the free electron density in the plasma lens. Such a gradient is present in the y direction but not in the x direction due to the elongation of the lens.

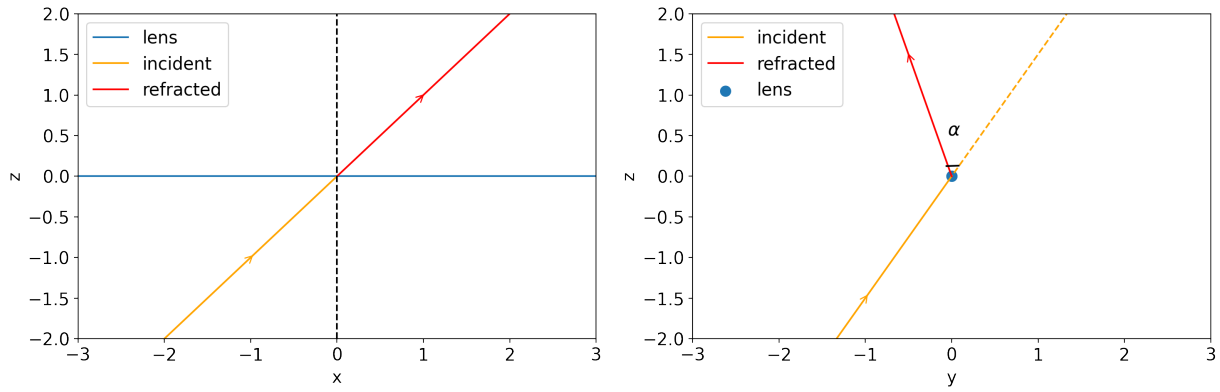

Figure 4.18: Refracted ray by a linear lens. The lens is extended along x axis, namely $z = y = 0$. Left: projection onto the plane $y = 0$, the direction of propagation for the ray does not change in the x direction. Right: projection onto $x = 0$, the ray is deflected by an angle α in y direction.

When linear lenses are present on multiple screens that are perpendicular to the line of sight, a ray refracted by a set of specified lenses connecting the pulsar to the observer can be solved as a linear algebra problem. We refer the readers to van Kerkwijk 2021 (external link) for a detailed derivation in the context of this problem. We show a simulation result below for a scattering geometry analogous to the data set in Figure 4.19. The 1 ms feature arises naturally in such a geometry, and it manifests as an offset parabola in the wavefield. The bottom of this offset parabola corresponds to the singly scattered ray by the lens on screen 2, as it is the minimum in delay. The corresponding image of this singly scattered ray moves along a parabola centered at the origin with a predicted velocity by the argument in section 2.4.1. We will show that the temporal evolution of the observed spectra follows this prediction.

4.5 Reconstructing Scattering Geometry

Recall from section 2.4.1 that an image produced by an linear lens (or the apex of an arclet) moves in the secondary spectrum along a parabola with speed:

$$\dot{f}_D = \frac{\lambda}{2c}\frac{1}{\eta}\,, \tag{4.2}$$

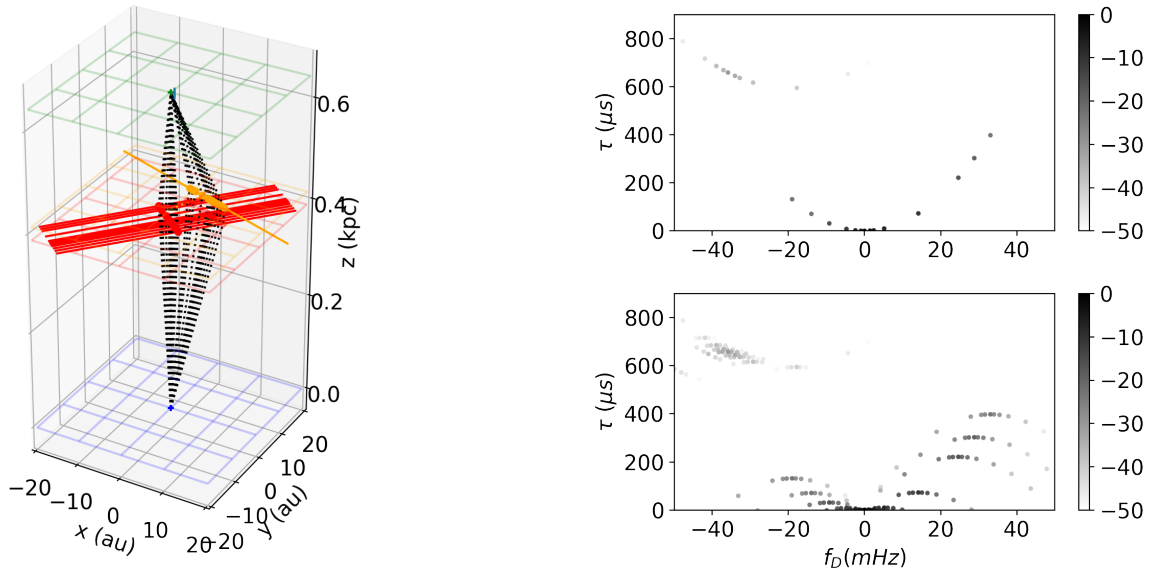

Figure 4.19: The proposed scattering geometry (left), the resulting wavefield (upper right), and the secondary spectrum (lower right). The parameters used for the lenses are comparable with those observed. In the left plot, the pulsar is at the top and the observer is at the bottom. Lenses on screen 1 are represented in red, those on screen 2 in orange. The rays are drawn in dashed lines. We see two bundles of rays. Those on the left are singly scattered rays by screen 1, whereas those on the right are doubly scattered rays by both screens, which gives rise to the 1 ms feature in the wavefield and secondary spectrum.

where η is the curvature of the parabola. The above prediction only applies to singly scattered images. On MJD 53712, the bottom of the offset parabola in the 1 ms feature becomes visible. Recall from the last section that the bottom of the offset parabola corresponds to the singly scattered image by the lens on screen 2. Therefore, the bottom of this offset parabola is constrained to move along another parabola through the origin. We fit the coordinate of the offset parabola by eye and evaluate the curvature. We show the resulting fit in Figure 4.20. The blue dot is the best fit, with the two red dots indicating uncertainty in the Doppler frequency. Uncertainty in the delay is negligible compared with that in the Doppler frequency. The blue and red curves are parabolas, centered at the origin, passing through the blue and red dots respectively. The curvature of the parabola is measured to be 0.91(7) s^3.

Assuming that the curvature does not vary significantly over the 7 weeks of observations, we may use Eqn 4.2 to extrapolate the position for the bottom of the offset parabola, or the singly scattered image by screen 2, to previous observation dates. The results are shown in Figure 4.21, where we overplot parabolas with a fixed curvature centered at the extrapolated positions for all 7 epochs. Note that all the overplotted parabolas and dots are based only on the coordinates for the blue dot measured by eye in Figure 4.20. The resulting extrapolation is an excellent fit to the data throughout the 7 weeks.

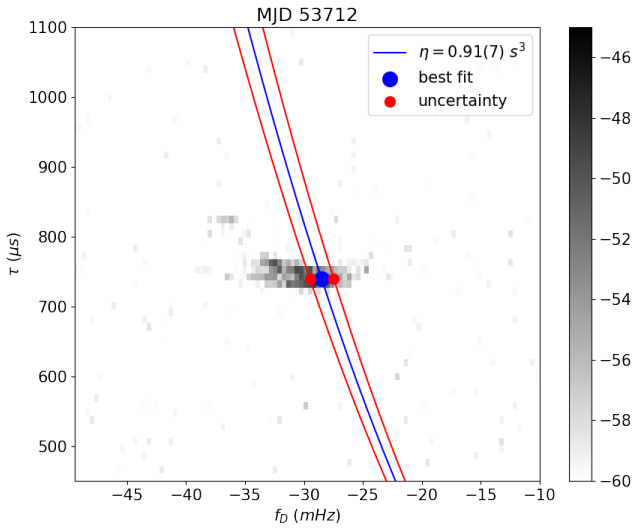

Figure 4.20: Identifying the bottom of the 1 ms feature by eye on MJD 53712.

We do not see the bottom of the lens, or singly scattered rays, in previous observations as the lens terminated before the singly scattered image can be produced. In other words, the observations are showing one end of a highly elongated lens that is causing the 1 ms feature. As the pulsar gradually approaches this lens, the singly scattered ray becomes visible in the last two epochs.

We may also extrapolate forward to find the time when the bottom of this offset parabola is at the origin. That date is identified to be MJD 53903, 191 days after the last observation. We know that on that date, the pulsar was directly behind this lens. Given that the lens is linear, we may identify the orientation of the lens by drawing a straight line between the sky location of the singly scattered image on MJD 53712 and the pulsar location on MJD 53903. The resulting geometry is given in Figure 4.22. We note that the measured images on the 1 ms feature (orange dots) lies slightly outwards from the inferred lens (blue line). This is expected since we assumed that all the images are singly scattered at the location of screen 1 when obtaining the discrete images in section 4.3.4. Recall that this assumption yields reasonable results as the two screens are very close compared to the distance between the pulsar and the observer.

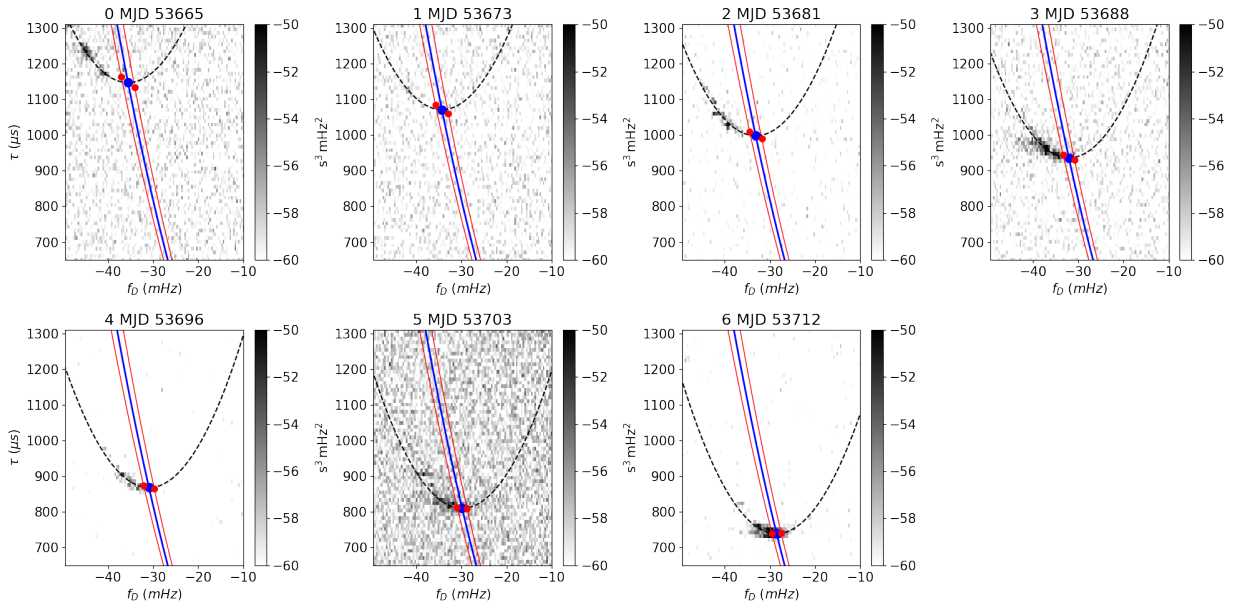

Figure 4.21: The predicted location for the offset parabola at each observation, all based on a measurement of the bottom of the offset parabola on MJD 53712 (see Figure 4.20).

4.6 Interpretation

In summary, we present strong evidence that the 1 ms feature in the seven observations are caused by an isolated and highly anisotropic lens that is moving slowly with respect to Earth ($\lessapprox$ 20 km/s). Based on the distance to the lens (415 pc), distance to the pulsar (620 pc), and the highest delay associated with the lens (1.25 ms), we estimate the lower bound for its deflection angle to be 83 mas at 318.5 MHz. Given typical interstellar electron densities, this is an *enormous* scattering angle. The angular width of the lens is found to be 1 mas. In order to be responsible for an ESE at a certain frequency, the deflection angle must be larger than the apparent angular width of the lens. For a plasma lens, the deflection angle is proportional to inverse frequency squared. The above parameters yield a lower bound of 2.6 GHz for the maximum frequency that the lens can cause an ESE. This is sufficient to explaining the majority of the observed ESEs over 2 GHz. Through the deflection angle, we estimate the plasma frequency to be 162(20)MHz, with the assumption that the lens takes on the shape of a prism and is perpendicular to the line of sight. We further infer the electron density to be 324(40) cm^{-3}. The inferred electron density may dramatically decrease if the plasma lens is inclined along the line of sight.

The width of the lens is found to be 0.5 AU. Combined with the relative velocity between the lens and the Earth, the lower bound for the time scale of a resulting ESE is found to be 44 days comparable with the 50 days time scale reported in Fiedler et al. (1987). Such a lens, when passing through the foreground of a quasar, inevitably causes an ESE.

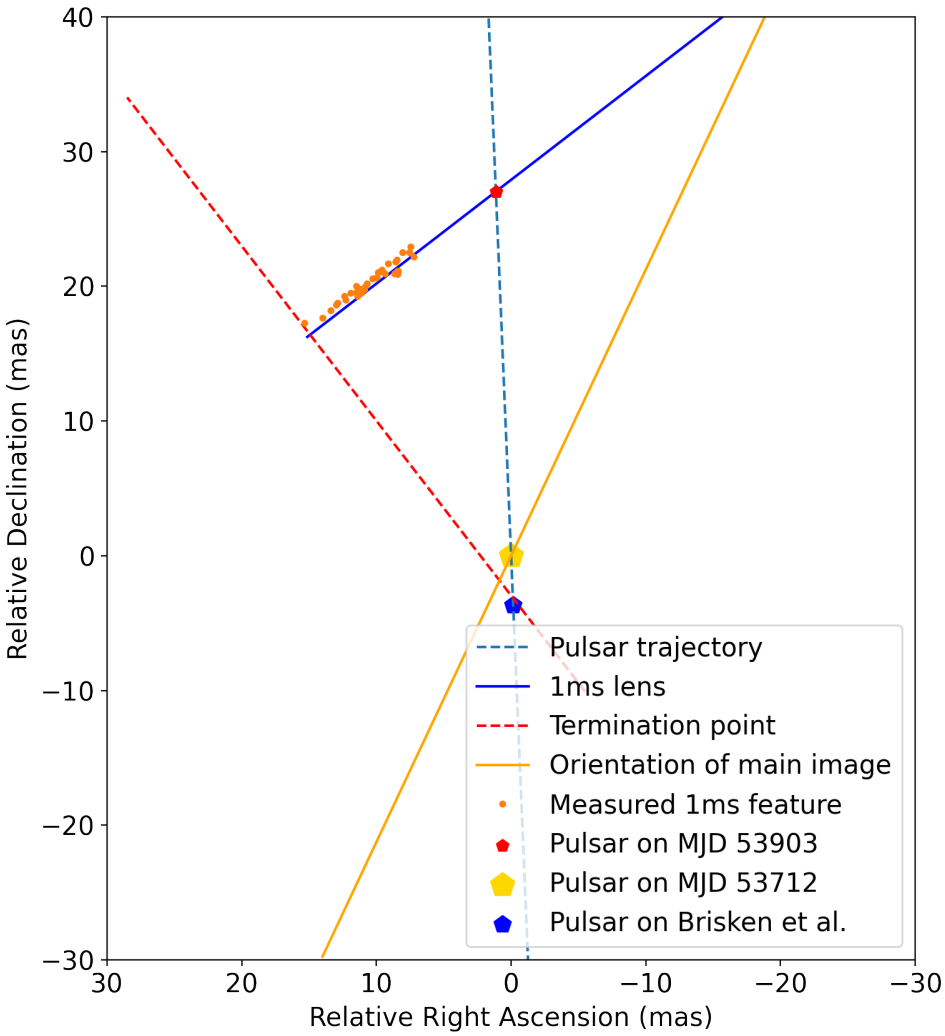

Figure 4.22: Inferred scattering geometry. The blue line indicates the orientation of the 1 ms lens on screen 2 obtained by drawing a straight line between the sky location of the singly scattered image on MJD 53712 and the pulsar location on MJD 53903. The orange dots are the measured discrete images on the 1 ms feature presented in Figure 4.17 after a coordinate transformation. The red dashed line indicates the termination point for the 1 ms lens. The singly scattered image by that lens disappear when the pulsar is below the intersection between the red dashed line and the pulsar trajectory.

Chapter 5

Conclusion

5.1 Summary of Results and Discussion

We reported the discovery of an exceptionally strong, isolated, and highly anisotropic plasma lens in the interstellar medium through a double lensing event of pulsar B0834+06 observed at the Arecibo Observatory. By analyzing the scintillation pattern, we reconstructed the holographic image of the pulsar refracted by the lens. Through temporal evolution over seven epochs, we confirmed that the lens is moving slowly with respect to Earth. Based on all the inferred parameters, this a lens can unambiguously cause a quasar extreme scattering event.

One difficulty remains. While the inferred electron density of the lens is small (~ 300 cm^{-3}) compared with previously proposed models ($10^3 \sim 10^5$ cm^{-3}), the overpressure problem remains. But we note that the above estimate comes with the assumption that the lens is perpendicular to the line of sight; the inferred electron density would decrease dramatically if the lens is at a grazing angle.

5.2 Future Work

This work demonstrates the power of using pulsar as a precision probe of the interstellar medium. Some promising future work includes:

1. We can solve for the distance to a pulsar if such a lensing event occurs for a pulsar in a binary system.
2. We may apply the phase-retrieval technique to better estimate the delay of the pulsar signals due to interstellar propagation. This is crucial for low-frequency gravitational wave detection based on pulsar timing.
3. We can apply the theta-theta mapping to a large archive of secondary spectra created by Prof. Dan Stinebring.

4. Such lensing events can potentially be used to probe the pulsar magnetosphere (Pen et al., 2013; Marshall & Clark, 1984).

5. We will propose observations of the pulsar B0834+06 with the FAST telescope in China. With state-of-the-art sensitivity and wide bandwidth, FAST will reveal more interesting structures in the interstellar medium.

References

Baker, D., van Kerkwijk, M., Main, R., et al. 2021, submitted

Brisken, W. F., Macquart, J.-P., Gao, J. J., et al. 2010, ApJ, 708, 232

Clegg, A. W., Fey, A. L., & Lazio, T. J. W. 1998, , 496, 253

Condon, J. J., & Ransom, S. M. 2016, Essential Radio Astronomy

Cordes, J. M., & Rickett, B. J. 1998, 507, 846

Cordes, J. M., Rickett, B. J., Stinebring, D. R., & Coles, W. A. 2006, 637, 346

Cordes, J. M., & Wolszczan, A. 1986, 307, L27

Demorest, P. B. 2011, 416, 2821

Fey, A. L., Clegg, A. W., & Fiedler, R. L. 1996, , 468, 543

Fiedler, R. L., Dennison, B., Johnston, K. J., & Hewish, A. 1987, 326, 675

Goldreich, P., & Sridhar, S. 2006, The Astrophysical Journal, 640, L159–L162

Gwinn, C. R. 2019, , 486, 2809

Heger, A., Fryer, C. L., Woosley, S. E., Langer, N., & Hartmann, D. H. 2003, The Astrophysical Journal, 591, 288–300

Hill, A. S., Stinebring, D. R., Asplund, C. T., et al. 2005, ApJL, 619, L171

Lee, L. C. 1976, , 206, 744

Liu, S., Pen, U.-L., Macquart, J.-P., Brisken, W., & Deller, A. 2016, , 458, 1289

Lorimer, D. R., & Kramer, M. 2005, Handbook of Pulsar Astronomy (Cambridge University Press)

Lorimer, D. R., & Kramer, M. 2012, Handbook of Pulsar Astronomy

Marshall, F. J., & Clark, G. W. 1984, 287, 633

Pen, U.-L., & King, L. 2012, , 421, L132

Pen, U.-L., & Levin, Y. 2014, MNRAS, 442, 3338

Pen, U.-L., Macquart, J. P., Deller, A., & Brisken, W. 2013, ArXiv 1301.7505, arXiv:1301.7505

Pen, U.-L., Macquart, J.-P., Deller, A. T., & Brisken, W. 2014, , 440, L36

Pushkarev, A. B., Kovalev, Y. Y., Lister, M. L., et al. 2013, , 555, A80

Rickett, B. J. 1977, , 15, 479

—. 1990, , 28, 561

Rickett, B. J., Lyne, A. G., & Gupta, Y. 1997, 287, 739

Rickett, B. J., Stinebring, D. R., Zhu, H., & Minter, A. H. 2021, , 907, 49

Romani, R. W. 1988, in American Institute of Physics Conference Series, Vol. 174, Radio Wave Scattering in the Interstellar Medium, ed. J. M. Cordes, B. J. Rickett, & D. C. Backer, 156–162

Simard, D., & Pen, U.-L. 2018, MNRAS, 478, 983

Simard, D., Pen, U. L., Marthi, V. R., & Brisken, W. 2019, , 488, 4963

Sprenger, T., Wucknitz, O., Main, R., Baker, D., & Brisken, W. 2021, , 500, 1114

Stinebring, D. R., McLaughlin, M. A., Cordes, J. M., et al. 2001, 549, L97

Stinebring, D. R., Rickett, B. J., & Koch Ocker, S. 2019, , 870, 82

Walker, M., & Wardle, M. 1998, ApJ letter, 498, L125

Walker, M. A., Demorest, P. B., & van Straten, W. 2013, ApJ submitted

Walker, M. A., Koopmans, L. V. E., Stinebring, D. R., & van Straten, W. 2008, , 388, 1214

Walker, M. A., Melrose, D. B., Stinebring, D. R., & Zhang, C. M. 2004, MNRAS, 354, 43

Walker, M. A., & Stinebring, D. R. 2005, MNRAS, 362, 1279